Atmos. Chem. Phys. Discuss., https://doi.org/10.5194/acp-2018-337
Manuscript under review for journal Atmos. Chem. Phys.
Discussion started: 15 May 2018
© Author(s) 2018. CC BY 4.0 License.

Atmospheric Chemistry and Physics Discussions

Lagrangian simulation of ice particles and resulting dehydration in the polar winter stratosphere

Ines Tritscher[1], Jens-Uwe Grooß[1], Reinhold Spang[1], Michael C. Pitts[2], Lamont R. Poole[3], Rolf Müller[1], and Martin Riese[1]

[1]Institute of Energy and Climate Research: Stratosphere (IEK-7), Forschungszentrum Jülich, 52425 Jülich, Germany
[2]NASA Langley Research Center, Hampton, Virginia 23681, USA
[3]Science Systems and Applications, Inc., Hampton, Virginia, 23666, USA

Correspondence: Ines Tritscher (i.tritscher@fz-juelich.de)

Abstract. Polar ozone loss in late winter and early spring is caused by enhanced concentrations of active chlorine. The surface necessary for heterogeneous reactions activating chlorine species is provided by cold stratospheric aerosols and polar stratospheric clouds (PSCs). Moreover, sedimentation of PSC particles changes the chemical composition of the lower stratosphere and alters the process of ozone depletion by irreversible redistribution of nitric acid and water vapor.

The Chemical Lagrangian Model of the Stratosphere (CLaMS) simulates the nucleation, growth, sedimentation, and evaporation of PSC particles along individual trajectories. Particles consisting of nitric acid trihydrate (NAT) were the focus of previous work and are known for their potential to denitrify the polar stratosphere. Here, we carried this idea forward and introduced the formation of ice PSCs and the related dehydration within the sedimentation module of CLaMS.

We show results from the Arctic winter 2009/2010, which is already well characterized because of the RECONCILE aircraft campaign and connected work. CLaMS simulations from the Antarctic winter 2011 complete this study and demonstrate the model's performance over an entire PSC season in the Southern Hemisphere. For both hemispheres, we present CLaMS results in comparison to PSC observations from the Cloud-Aerosol Lidar with Orthogonal Polarization (CALIOP) and the Michelson Interferometer for Passive Atmospheric Sounding (MIPAS). Moreover, we confront CLaMS simulations of water vapor with vortex-wide Microwave Limb Sounder (MLS) observations. Observations and simulations are compared on season-long and vortex-wide scales as well as for single PSC events. The simulations reproduce well both the timing and extent of PSC occurrence inside the entire vortex. Divided into specific PSC classes, CLaMS results show good agreement with CALIOP and MIPAS observations, even for specific days and single satellite orbits. The vertical redistribution of nitric acid and water during the polar winter season, as seen in the MLS data, is visible in the CLaMS data as well. Overall, a conclusive agreement between CLaMS and a variety of independent measurements is presented.

1 Introduction

The representation of polar stratospheric clouds (PSCs) in global models is often poor despite their importance for ozone chemistry in polar winter and spring. In the lower stratosphere, PSCs provide surfaces for heterogeneous reactions activating chlorine species and thus accelerating ozone loss (Solomon et al., 1986; Solomon, 1999). Even though the importance

© Author(s) 2018. CC BY 4.0 License.

of liquid particles with respect to chlorine activation and ozone depletion has been shown in recent publications, (Drdla and Müller, 2012; Wohltmann et al., 2013; Kirner et al., 2015), also solid particles influence heterogeneous chemistry substantially (Solomon et al., 2015). Sedimentation of solid PSC particles irreversibly change the chemical composition of the lower stratosphere and alters the process of ozone depletion by denitrification (Fahey et al., 2001; Molleker et al., 2014) and dehydration (Kelly et al., 1989). Moreover, model results for each type of particle are not additive in a simple way as shown by Solomon et al. (2015). Therefore, particle surface areas in models should be described as precise and realistic as possible.

Thanks to the Montreal Protocol and its amendments and adjustments, concentrations of ozone depleting substances are now decreasing continuously (WMO, 2014) and Solomon et al. (2016) now present evidence that the healing of the Antarctic ozone layer has actually started. However, recent years showed new record ozone losses above the Arctic winter pole (Manney and Lawrence, 2016), a crucial reason to still step up efforts in understanding and modeling PSC formation on global scales better. Facing climate change, an in depth understanding of atmospheric processes becomes even more important and a complete and comprehensive knowledge of processes affecting stratospheric ozone is required to reliably predict the future evolution of the ozone layer.

PSCs are supposed to consist of liquid supercooled ternary solution (STS) droplets, solid nitric acid trihydrate (NAT) particles and/or solid ice particles (Peter and Grooß, 2012). Their formation mechanisms are still a focus of research, newly motivated by global, high resolution satellite observations (Spang et al., 2018; Pitts et al., 2018). Due to the level of complexity and still existing knowledge gaps, large differences in the parameterization and representation of PSCs in global models exist. Most current global models use a simplified PSC scheme that prescribes number densities and particle radii and assumes thermodynamical equilibrium (Morgenstern et al., 2017). Some Chemistry Climate Models (CCMs) like SD-WACCM and EMAC (ECHAM5/MESSy Atmospheric Chemistry model) offer submodels with more detailed PSC schemes. Those can be coupled to the standard model setup for intensive PSC studies, as done by Kirner et al. (2011, 2015) with EMAC and Zhu et al. (2015, 2017b, a) with SD-WACCM. However, as presented recently by Khosrawi et al. (2018), comparisons of measured PSC properties with corresponding EMAC results show deficiencies. Before Zhu et al. (2017a), the microphysical model for ice particles within SD-WACCM was missing and the fact that NAT nucleation in SD-WACCM is still based on the homogeneous surface nucleation scheme by Tabazadeh et al. (2002) is a matter of debate (Peter and Grooß, 2012). Gaps, weaknesses, and uncertainties exist even in advanced PSC schemes and they further motivated our current research.

Here, we present new developments extending the sedimentation module of the Chemical Lagrangian Model of the Stratosphere (CLaMS). We added ice PSC particles to complete the PSC scheme, which allows comparisons to PSC measurements and simulations of de- and rehydration in Arctic and Antarctic. To demonstrate the performance of the new CLaMS ice sedimentation module, we have chosen two distinct winters, one Arctic and one Antarctic winter. The Arctic winter 2009/2010 shows widespread ice PSCs during mid of January and is therefore ideally suited to test our new ice scheme. Additionally, the Arctic winter has been the focus of the intensive RECONCILE aircraft campaign, which took place from January till March

© Author(s) 2018. CC BY 4.0 License.

2010 (von Hobe et al., 2013). The 2011 Antarctic winter is representative for other Antarctic winters. Global satellite data from the Cloud-Aerosol Lidar with Orthogonal Polarization (CALIOP) (Pitts et al., 2018) and the Michelson Interferometer for Passive Atmospheric Sounding (MIPAS) (Spang et al., 2018) are available for both winters and allow a comprehensive evaluation of our model results, to be conducted.

2 CLaMS model description and setup

The Chemical Lagrangian Model of the Stratosphere (CLaMS) is a global, three-dimensional Chemical Transport Model (CTM) based on the Lagrangian principle (McKenna et al., 2002b, a; Konopka et al., 2004). CLaMS is structured into modules, which can individually be switched on and off as needed. The principal CLaMS modules are the trajectory module, the mixing module and the chemistry module. Within the CLaMS trajectory module, air parcels are advected forward in time based on prescribed wind fields. This study makes use of wind and temperature fields from ERA-Interim analysis provided by the European Centre of Medium-Range Weather Forecasts (ECMWF) (Dee et al., 2011). Total diabatic heating rates are also taken from ERA-Interim and used to determine vertical velocities (Ploeger et al., 2010). CLaMS uses a hybrid vertical coordinate (ζ). At pressure levels lower than 300 hPa, ζ can be interpreted as potential temperature (θ). Towards higher pressure levels, ζ transforms from an isentropic to a pressure-based coordinate (Pommrich et al., 2014). Mixing is induced where the underlying wind field shows large shear, diagnosed by the Lyapunov exponent (McKenna et al., 2002b). Wherever the Lyapunov exponent exceeds a critical value, mixing between air parcels is introduced either by adding or by merging air parcels in the case of divergence or convergence, respectively. Using this method, a critical Lyapunov exponent of $1.5\,\mathrm{day}^{-1}$ ensures an approximate equally distributed grid and appropriate mixing strength (McKenna et al., 2002b). The sensitivity of simulated trace gas distributions in the upper troposphere / lower stratosphere to the value of the critical Lyapunov coefficient is further discussed in Riese et al. (2012). Stratospheric chemistry within the CLaMS chemistry module is an updated version of McKenna et al. (2002a) with additional reactions listed in Grooß et al. (2014). The chemical composition of the whole atmosphere is described by the individual air parcels in the shown setup. Each air parcel represents a certain volume of its surrounding atmosphere with about 380 000 air parcels in total. Here, simulations were carried out with a horizontal resolution of 100 km in the polar regions. Vertically, the model is divided into 32 levels between 320 and 900 K, resulting in a vertical resolution of about 700 m between 20 and 25 km altitude. The chemical initialization of the hemispheric runs starting on 01 December 2009 and 01 May 2011, respectively, was based on satellite data and observed tracer correlations (Grooß et al., 2014). Additionally, we used data from a multi-annual CLaMS simulation with simplified chemistry (Pommrich et al., 2014). The details for the individual species are given in Grooß et al. (2014) for the Arctic winter 2009/2010 and in Grooß et al. (2018) for the Antarctic winter 2011.

The CLaMS cirrus module is used in the regular CLaMS setup to calculate the dehydration of air masses at the tropopause level. This mechanism can be implemented by either using a temperature dependent parametrization for heterogeneous ice freezing (Krämer et al., 2009) or by a fixed value of 100 % for saturation over ice. Water ice is removed if the inferred particle fall speed exceeds a prescribed threshold value. This parametrization also allows dehydration in the stratosphere to be simulated

© Author(s) 2018. CC BY 4.0 License.

(e.g. Grooß et al., 2014). However, it does not allow for simulations of vertical redistribution of water, since water is irreversibly removed once a critical fall speed is exceeded. Therefore, we restricted the cirrus module to the troposphere ($\zeta < 380\,\mathrm{K}$ and PV < 2) within this study with an ice freezing threshold of $100\,\%$. Within the stratosphere, the new ice parameterization of the sedimentation module takes over.

2.1 Sedimentation module

The CLaMS sedimentation module offers the possibility to enhance simulations of the polar winter stratosphere by PSC cloud formation and corresponding particle sedimentation. The module has been developed by Grooß et al. (2005) and was so far limited to the formation of NAT particles. Within this study, we expand the sedimentation module to the simulation of ice PSC particles. This step enables now the simulation of water redistribution. Moreover it provides the opportunity for detailed comparisons of simulated PSC properties with various observations. Finally, NAT and ice particle surface areas are calculated within the CLaMS sedimentation module and now also transfered to and used within the chemistry module. First applications are shown in a paper by Grooß et al. (2018).

Sedimenting particles in CLaMS are also described by a Lagrangian approach. So-called particle parcels are initialized next to CLaMS air parcels and move independently within the three-dimensional space. Every particle parcel represents a number of NAT or ice particles, equally distributed over a certain volume of air. The given number density remains constant during the particle's lifetime. Growth, sedimentation, and evaporation of the particles are carried out following the procedure described in detail in Carslaw et al. (2002). Vapor pressures of $\mathrm{HNO_3}$ are calculated following Hanson and Mauersberger (1988), $\mathrm{H_2O}$ vapor pressures are calculated according to Murphy and Koop (2005). Uptake and release of $\mathrm{H_2O}$ and $\mathrm{HNO_3}$ is carried out by taking into account a weighted distance to the three nearest neighbors each above and below (Konopka et al., 2004). Further details to the module's fundamentals can be found in Grooß et al. (2005).

Currently, the sedimentation module comprises the following nucleation pathways:

- Heterogeneous NAT nucleation

  Grooß et al. (2005) started the sedimentation module using a constant NAT nucleation rate taken from Voigt et al. (2005). With a rate of $7.8 \times 10^{-6}\,\mathrm{cm^{-3}h^{-1}}$, NAT formed instantaneously as soon as temperatures dropped below T_{NAT}. In Grooß et al. (2014), the heterogeneous NAT nucleation was updated motivated by results obtained in the RECONCILE field campaign and new scientific findings about heterogeneous PSC nucleation. According to Hoyle et al. (2013), a saturation-dependent, non constant nucleation rate of NAT particles was formulated and used to improve the simulations. The active site theory (Marcolli et al., 2007) represents the basis for this approach. The idea behind is that particles may offer a certain probability to nucleate NAT or ice, respectively. The probability differs from particle to particle, which leads to nucleation events over a broad temperature range as observed by Marcolli et al. (2007). So called active sites, particle surface inhomogeneities, are assumed to initiate nucleation. A particle might carry several of these sites

© Author(s) 2018. CC BY 4.0 License.

but only the best active site is of importance and triggers the nucleation event. For the use within CLaMS, the number of particles carrying a particular contact angle is tabulated in steps of 0.1° and described by a combination of temperature and saturation ratio. The nucleation rate is calculated by the sum over all bins up to the actual temperature and saturation ratio. Further particle nucleation takes place only if the temperature drops and/or the saturation ratio increases.

Compared to Grooß et al. (2014), we changed two details in the calculation. (1) Information related to the number of activated contact angles are stored for each particle parcel and are now also exchanged with the surrounding air parcels. Increasing saturation ratios increases the number of activated contact angles. Mixing is considered and as soon as PSC particles evaporate, the value for activated contact angles is reset to zero. (2) Up to now, particle formation took place every 24 hours (Grooß et al., 2014). For this reason, $S_{\mathrm{NAT/ICE}}$ and T_{min} are traced along each air parcel trajectory to make use of the daily minimum temperature and maximum saturation ratio. We kept the possibility to nucleate PSC particles only once per day, e.g. to save computing time, but introduced now also the possibility to use an hourly nucleation timestep. In this case, hourly resolved values of temperature and $S_{\mathrm{NAT/ICE}}$ are taken to calculate nucleation rates of NAT and/or ice particles.

– Heterogeneous ice nucleation

Heterogeneous ice nucleation has been implemented within CLaMS in analogy to heterogeneous NAT nucleation. Vapor pressures for ice are calculated following Murphy and Koop (2005). Depending on temperature and supersaturation with respect to ice (S_{ice}), a fixed number of ice particles may nucleate. Ice particle number densities are determined with the help of a look-up table, as done in Grooß et al. (2014) for heterogeneous NAT nucleation. The look-up table is illustrated in Fig. 1 and based on the same parameterization for heterogeneous ice nucleation as defined in Engel et al. (2013). A combination of temperature (x-axis) and supersaturation (color-coded) defines the number of foreign nuclei initiating ice particle nucleation, which is therefore equal to the number of nucleated ice particles (y-axis on the right side of the figure). With decreasing temperature and increasing supersaturation, more contact angles can be activated (y-axis on the left side of the figure) and the number density of nucleated ice particles increases. The size of the nucleated ice particles is often determined by equilibrium conditions. While nitric acid uptake for micron-sized particles needs hours, water is in equilibrium on the timescales of seconds (Meilinger et al., 1995). The water fraction in ice particles is calculated as the difference of the total partial pressure of water and the saturation vapor pressure of water over ice, depending on pressure and temperature.

The look-up table, as well as the parameterization from Engel et al. (2013), requires the existence of small-scale temperature fluctuations. Those have been introduced into CLaMS as described in Sec. 2.2. The use of synoptic-scale temperatures only, as provided by ERA-Interim, would require a reduction of the nucleation barrier. We performed several sensitivity runs with different starting contact angles (not shown) and concluded that values of S_{ice} need to be lowered by about 0.17 to compensate missing temperature fluctuations and to achieve similar results for PSC occurrence and de-

© Author(s) 2018. CC BY 4.0 License.

hydration. However, higher cooling rates as provided by smaller scale temperature fluctuations resolve individual PSCs better.

– Homogeneous ice nucleation

Homogeneous nucleation of ice crystals from supercooled aqueous solution droplets has been described by Koop et al. (2000). To calculate the freezing threshold within CLaMS, we introduced the critical supersaturation S_{cr} following Kärcher and Lohmann (2002):

$$S_{\mathrm{cr}} = 2.583 - \frac{T[K]}{207.83} \tag{1}$$

This approximation is based on Koop et al. (2000) and saves additional computation time. The particle radius of 0.25 µm given by Kärcher and Lohmann (2002) agrees well with the mean radius of STS droplets (Peter and Grooß, 2012). Homogeneous ice nucleation requires a supercooling of 3 to 4 K compared to the ice frost point (Koop et al., 2000; Daerden et al., 2007) and therefore high supersaturations at stratospheric polar winter conditions (S_{cr} is nearly constant at about 1.7 in the temperature range from $\sim$ 180 - 190 K (Maturilli and Dörnbrack, 2006)). Such conditions can be found e.g. above orographic mountains. The entire background aerosol of $10\,\mathrm{cm}^{-3}$ may freeze in wave events with high cooling rates (e.g. Carslaw et al., 1998a; Fueglistaler et al., 2003). Therefore, we assume that homogeneous nucleation within CLaMS results in $n(\mathrm{ice}) = 10\,\mathrm{cm}^{-3}$.

– NAT nucleation on preexisting ice particles

NAT nucleation on preexisting ice particles is an accepted and often confirmed pathway of NAT formation (Carslaw et al., 1998b; Biermann et al., 1998; Luo et al., 2003). Downstream of mountain waves, NAT supersaturations are high and clouds with NAT number densities of up to $1\,\mathrm{cm}^{-3}$ have been observed (see Peter and Grooß, 2012, and references therein). In this study, we allow 50 % of the existing ice particles to serve as NAT nucleus with an upper limit of $n(\mathrm{NAT}) = 1\,\mathrm{cm}^{-3}$ per nucleation event. NAT particle radii and volume are determined assuming thermodynamical equilibrium. This calculation is a first and easy attempt to include NAT nucleation on preexisting ice particles in a global model and may need refinements in later studies.

2.2 Parametrization of temperature fluctuations

It has been shown in several studies that small-scale temperature fluctuations are ubiquitous in the atmosphere and play an important role in ice cloud formation (e.g. Hoyle et al., 2005; Kärcher et al., 2014; Podglajen et al., 2016). Even if synoptic-scale temperatures are above PSC formation thresholds, negative temperature excursions may trigger ice cloud formation and rapid cooling rates may change cloud characteristics. Orographicly induced temperature fluctuations are focus of several Arctic (e.g. Carslaw et al., 1998b; Dörnbrack et al., 2002) and Antarctic research studies (e.g. Höpfner et al., 2006a; Alexander et al., 2011; Noel and Pitts, 2012; Orr et al., 2015) on PSCs. Observations from the Atmospheric Infrared Sounder (AIRS)

© Author(s) 2018. CC BY 4.0 License.

were used by Hoffmann et al. (2017) to evaluate explicitly resolved temperature fluctuations due to gravity waves in high-resolution meteorological analyses. Even though wave amplitudes are typically underestimated, Hoffmann et al. (2017) found that observed gravity wave patterns agree well with those simulated in the ECMWF operational analysis. Due to a resolution of $1^\circ \times 1^\circ$ of the underlying wind and temperature fields from ERA-Interim used in this study, we do not expect to explicitly catch wave patterns such as mountain wave ice events (see e.g. Engel et al., 2013). However, a persistence of gravity wave activity from background winds at subgrid-scales need to be parameterized somehow in order to mimic PSC formation in general.

For CLaMS, we make use of parameterizations by Gary (2006) for the Northern Hemisphere (NH) and Gary (2008) for the Southern Hemisphere (SH), respectively. Gary (2006) showed that mesoscale temperature fluctuations increase with altitude in a systematic way. They are greatest over mountainous terrain and towards polar latitudes during winter. These dependencies are expressed in the following equations to calculate mesoscale fluctuation amplitudes (MFA), that are not present on synoptic scales:

$$\text{MFA (NH)} = (112 - 1.21\ \text{Latitude} + 2.20\ W \cdot \text{Latitude} + 29.0\ \text{Topography}) \cdot \frac{\text{Pressure [hPa]}}{58.85}^{-0.4} \tag{2}$$

$$\text{MFA (SH)} = (114 - 0.42\ \text{Latitude} + 0.84\ W \cdot \text{Latitude} + 29.0\ \text{Topography}) \cdot \frac{\text{Pressure [hPa]}}{58.85}^{-0.4} \tag{3}$$

Taking negative latitudes for the SH, we assumed a mean topographic parameter of 0.5. Equation 4 represents a corrected version of the original Equation (3) of Gary (2006) (Bruce Gary, private communication). Consequently, the parameter W is calculated for each day of the year (DOY) and both hemispheres in the following way:

$$W = 0.5 \cdot \left[1 + \sin\left(2\pi \cdot \frac{\text{DOY} - 295}{365}\right)\right] \tag{4}$$

MFA is first converted from full-width to half-width amplitude and also from its original altitude unit m to the temperature unit K by a simple conversion assuming a dry adiabatic temperature behavior of $1\,\mathrm{K} = 100\,\mathrm{m}$. MFA is further scaled by random numbers originating from a normal distribution, with MFA being the standard deviation. The resulting temperature is added to the ERA-Interim synoptic-scale temperature and used for the calculations of particle nucleation.

3 Comparison to measurements

To evaluate simulations from the new ice PSC scheme within the CLaMS sedimentation module, we compare our results with satellite measurements from the Cloud-Aerosol Lidar with Orthogonal Polarization (CALIOP), the Microwave Limb Sounder (MLS), and the Michelson Interferometer for Passive Atmospheric Sounding (MIPAS). Since April 2006, CALIOP flies on the CALIPSO satellite measuring high resolution backscatter profiles from which information about PSC composition can be inferred. MLS has been launched already in July 2004 on the Aura spacecraft and delivers profiles of HNO_3 and H_2O. As

© Author(s) 2018. CC BY 4.0 License.

part of the NASA/ESA A-Train constellation, both instruments closely follow each other along the same track describing a sun-synchronous polar orbit with a global coverage ranging from 82° N to 82° S (Stephens et al., 2002; Waters et al., 2006). MIPAS was operating on board the Envisat satellite from July 2002 to April 2012 measuring limb infrared (IR) spectra in the wavelength range from 4 to 15 µm (Fischer et al., 2008). The satellite operated also in a sun synchronous orbit and allowed geographical coverage up to both poles due to additional poleward tilt of the primary mirror (usually 87° S to 89° N). MIPAS measures PSCs at day and night time.

3.1 CALIOP

During the last decade, CALIOP was the basis of various studies on PSCs. The Level 2 PSC Mask Product Version 1.0 (v1) is based on PSC detection and classification as described in Pitts et al. (2011). Within this study, we make use of Version 2.0 (v2) of the PSC product, which has recently been introduced in Pitts et al. (2018). PSCs are detected as statistical outliers relative to the background stratospheric aerosol population (at $T < 200\,\mathrm{K}$) in perpendicular backscatter (β_{perp}) or scattering ratio (R). The background threshold values ($R_{\text{threshold}}$ and $\beta_{\text{perp,threshold}}$) are defined as median plus one median absolute deviation. The thresholds are daily values that vary with potential temperature and are listed in the CALIOP v2 PSC data files. A CALIOP data point is defined to be a PSC if either $\beta_{\text{perp}} > \beta_{\text{perp,threshold}} + \sigma(\beta_{\text{perp}})$ or $R > R_{\text{threshold}} + \sigma(R)$ exceeds the background threshold plus an uncertainty (σ). An outlier in β_{perp} is assumed to contain detectable non-spherical particles. The optical space for non-spherical particles is divided into two general regimes. A dynamical boundary (R_{NATice}) separates NAT mixtures from ice. R_{NATice} is computed from estimates of cloud-free MLS $\mathrm{HNO_3}$ and $\mathrm{H_2O}$ vapors to account for effects of dehydration and denitrification. A data point is classified as ice if $R > R_{\text{NATice}}$ and $R < 50$, and is further classified as wave ice if $R > 50$. NAT mixtures are defined opposite of the dynamical boundary with values of $R < R_{\text{NATice}}$. Any NAT mixture with $R > 2$ and $\beta_{\text{perp}} > 2 \times 10^{-5}\,\mathrm{km^{-1}sr^{-1}}$ belongs to the sub-class named "enhanced NAT mixtures". Each data point that is not an outlier in β_{perp}, but is an outlier in R, is classified as STS. A visualization of the PSC classification can be found in the lower panels of Figs. 3 and 7. Please refer to Pitts et al. (2018) for more details of the v2 PSC classification.

A comparison of individual PSC clouds simulated within CLaMS and measured by CALIOP requires a conversion of model results into optical parameters. For every CALIOP data point, we compute a size distribution from CLaMS PSC particles within a radius of 50 km around the point of measurement and attribute this to the observation. As in Hoyle et al. (2013) and Engel et al. (2013), we make use of Mie theory and T-Matrix calculations to compute scattering of light by STS, NAT and ice particles as a function of wavelength (e.g. Mishchenko et al., 2010). Prolate spheroids for both ice and NAT particles with aspect ratios of 0.9 (diameter-to-length ratio) and a refractive index of 1.31 for ice and 1.48 for NAT have been chosen (Engel et al., 2013). To fully adopt the procedure of PSC classification, we calculated σ also for modeled values using the CALIOP noise equation as follows:

$$\sigma(\beta) = \mathrm{CNF} \cdot \sqrt{\beta} \tag{5}$$

© Author(s) 2018. CC BY 4.0 License.

The CALIOP noise factor (CNF) combines different scaling factors into a single value for each CALIOP horizontal averaging scale. We have been using a CNF of 0.00102 for all our calculations, which corresponds to an horizontal average of 135 km and therefore a best case for detection. The calculations have been done with the assumption that the parallel and perpendicular components of molecular backscatter are 0.99634 and 0.00366 times the total molecular backscatter, respectively. Finally, the following relationship is used for $\sigma(R)$:

$$\sigma(R) = |R| \cdot \sqrt{\frac{\sigma^2(\beta_{\text{perp}}) + \sigma^2(\beta_{\text{parallel}})}{(\beta_{\text{perp}} + \beta_{\text{parallel}})^2} + (0.03)^2} \tag{6}$$

The last term accounts for assumed 3 % relative uncertainty in molecular backscatter.

The procedure described above is essential to compare individual optical properties on a cloud by cloud basis. Comparisons between CLaMS, CALIOP, and MIPAS showing PSC areal coverage have been performed using CLaMS PSC surface areas. Information about the surface area density of ice, NAT, and STS particles per volume of air is available for every CLaMS air parcel. The quantity is derived from CLaMS particle parcels and interpolated onto neighboring CLaMS air parcels using a distance depending weight at every time step during the simulation. This step saves computing time and allows an easier post processing of the model results for comparisons, which do not require individual size distributions. As lower boundaries, in accordance with the CALIOP detection thresholds, we use 3.3 $\mu m^2 cm^{-3}$ for STS droplets (Carslaw et al., 1994), 0.25 $\mu m^2 cm^{-3}$ for NAT, and 0.5 $\mu m^2 cm^{-3}$ for ice particles. Values exceeding those thresholds are counted as PSCs and as a specific composition class, respectively.

3.2 MIPAS

The MIPAS PSC detection and classification approach is based on the combination of the well-known two-color ratio method for IR limb measurements (Spang and Remedios, 2003), the cloud index, and multiple 2-D brightness temperature difference probability density functions (Spang et al., 2016). The so-called Bayesian Classifier combines the information content of various correlation diagrams of color ratios and brightness temperature differences covering several atmospheric window regions. Finally, the classifier estimates the most likely probability that either one of the three PSC types (ice, NAT, or STS) dominates the spectral characteristics of MIPAS or defines mixed-type clouds with intermediate probabilities (40 - 50 %). The MIPclouds processor for detection and cloud parameter retrieval is presented in detail in Spang et al. (2012). Spang et al. (2016) introduced the methodology of the Bayesian Classifier (v1.2.8) for PSC cloud types. The classification method has been applied to the complete MIPAS data set (Spang et al., 2018).

Within this paper, we compared horizontal distributions of PSC composition classes for both hemispheres on single days at constant levels of potential temperature. MIPAS data have been processed as described above. For CLaMS, we calculated trajectories from the model results to map those onto the MIPAS measurement locations. As done for the comparison of PSC areal coverage (see Sect. 3.1), we used information about the surface area density of ice, NAT, and STS particles from CLaMS. The same detection thresholds (3.3 $\mu m^2 cm^{-3}$ for STS droplets, 0.25 $\mu m^2 cm^{-3}$ for NAT, and 0.5 $\mu m^2 cm^{-3}$ for ice

© Author(s) 2018. CC BY 4.0 License.

particles) have been applied to classify CLaMS model results for the comparison with MIPAS. Please note, that vertical sampling differences between MIPAS (1.5 - 3 km) and CLaMS ($\sim$ 700 m) exist.

3.3 MLS

MLS provides atmospheric profiles of temperature and composition (including H_2O and HNO_3) via passive measurement of microwave thermal emission from the limb of the Earth's atmosphere (Waters et al., 2006). We use version 4.2 of MLS measurements. Information about vertical and horizontal along-track resolutions as well as precision and accuracy of the data can be found in Livesey et al. (2017). For comparisons with CLaMS, we interpolated MLS parameters onto ζ levels and calculated daily averages for certain levels and equivalent latitude bins with areas of equal size.

The MLS averaging kernel has also been taken into account for additional comparisons of CLaMS model data to satellite observations. As for the comparison with MIPAS, we calculated trajectories to transfer the model results to the measurement locations. Afterwards, we applied a weighting defined by the satellite's averaging kernels using pressure as the vertical coordinate and the logarithm of H_2O and HNO_3 mixing ratios (Ploeger et al., 2013). Further details about the MLS averaging kernels are discussed in Livesey et al. (2017).

4 Results

Within this section, we present CLaMS results for the 2009/2010 Arctic winter as well as for the 2011 Antarctic winter in comparison to satellite observations (Sect. 3). We show plots of daily averaged PSC areal coverage over the entire winter. We compare simulations to single cloud observations and we contrast simulated H_2O and HNO_3 with satellite measurements.

The 2009/2010 Arctic winter was on average relatively warm, however, an exceptional cold period from mid December until end of January led to the formation of widespread PSCs. At that time, the RECONCILE field campaign took place (von Hobe et al., 2013) and intensive PSC studies followed from this campaign. NAT and ice parameterizations by Hoyle et al. (2013) and Engel et al. (2013), respectively, are based on PSC observations during this particular winter. To demonstrate that both parameterizations are working within CLaMS as well as in the original Lagrangian Zurich Optical and Microphysical box Model (ZOMM), we selected the 18 January 2010 for a single cloud comparison because this day was analyzed in detail by Engel et al. (2013). Moreover, this day is right in the middle of the one week period of intensive ice cloud coverage in the NH vortex with largest areas covered by ice PSCs.

The 2011 Antarctic winter is amongst the colder Antarctic winters with a pronounced ozone hole (Klekociuk et al., 2014). Observations from MIPAS, CALIOP, and MLS are available throughout this entire winter. This is the first time that CLaMS simulations of dehydration and denitrification are shown in detail for a SH winter. For this reason, the Antarctic winter 2011 is presented with a series of cloud comparisons throughout the whole PSC season.

© Author(s) 2018. CC BY 4.0 License.

4.1 2009/2010 Arctic winter: comparison with observations

We start the presentation of CLaMS results with a season long and vortex wide comparison of PSC areal coverage. Daily, height resolved values of PSC areal coverage in the 2009/2010 Arctic winter are shown in Fig. 2. Between 55° and 90°, we defined eight latitude bands of equal area with widths that vary in latitude from 2.3° (250 km) up to 12.2° (1340 km). The occurrence frequencies (number of PSC detections divided by the total number of observations) has been calculated for each band and altitude grid box. The PSC areal coverage is estimated as the sum of the occurrence frequency multiplied by the total area. This approach has also been used by Spang et al. (2018) and Pitts et al. (2018) and bypasses the caveat of the irregular sampling density due to the orbit geometry. MIPAS observations and CLaMS simulations are only considered at latitudes $< 82°\,\mathrm{N/S}$ to mimic the latitudinal sampling coverage of CALIOP. The model performance at PSC altitudes for the overall winter is remarkably good (Fig. 2). PSC occurrence starts in mid of December and lasts until the end of January in both independent measurements as well as in the simulation. CLaMS shows two maxima in PSC areal coverage similar to CALIOP. Also the vertical extent agrees well between all three panels. MIPAS shows a striking maximum at altitudes below $15\,\mathrm{km}$ in the early winter period. Polar cirrus at the tropopause and volcanic aerosols of the Sarychev eruption in June 2009 introduce a bias in the PSC detection (Spang et al., 2018). Looking in particular at ice PSCs, CLaMS misses ice clouds in the first two weeks of January that are seen by both CALIOP and MIPAS. Those ice clouds are mountain wave induced ice events as shown by Pitts et al. (2011), caused by wave-driven temperature minima missing in the ERA-Interim data (see Fig. 8 in Engel et al., 2013). Starting in mid-January, as synoptic-scale temperatures fell below the frost point, large areas of ice PSCs also develop within CLaMS with an extension comparable to the observations.

A detailed look on individual clouds illustrates the performance of the CLaMS ice PSC scheme. In the middle of the one week period of synoptic-scale ice PSCs in January 2010, we selected the 18 January 2010 for a single cloud comparison (Fig. 3). This particular orbit has already been in the focus of Engel et al. (2013) to adjust the heterogeneous nucleation rates for ice. Whereas Engel et al. (2013) used the microphysical box model ZOMM, run on single trajectories and starting at most ten days before the point of observation, we are using a CTM in this study, initialized on 01 December 2009 and running for the whole winter 2009/2010. Despite those fundamental model differences, the result is convincing and the agreement between both models suggests a robust parameterization of heterogeneous ice nucleation. The cloud classification as well as the individual parameters of aerosol backscatter ratio $(R-1)$ and β_{perp} agree well with the CALIOP observations. The lower panels of Fig. 3 illustrate the v2 PSC classification scheme. The dashed lines are dynamical thresholds as mentioned in Sect. 3.1. Plotted are daily maximum values for $\beta_{\mathrm{perp,threshold}}$ and $R_{\mathrm{threshold}}$ and the daily mean for R_{NATice}.

A comparison to MIPAS is beneficial to validate the new CLaMS PSC scheme. A different measurement technique as well as the fact that MIPAS data has not been used to adjust the nucleation rate allows an independent quality check. Figure 4 presents the daily PSC distribution of the Bayesian classifier for 18 January 2010. The colored symbols represent the PSC classes, where in addition to the three main classes (ice, STS, NAT), a mixed type of STS and NAT (NAT_STS) particles is shown. As

© Author(s) 2018. CC BY 4.0 License.

described already in Sect. 3.2, CLaMS surface area densities have been mapped onto the MIPAS profile locations. The classification of CLaMS results is based on surface area densities, which need to be large enough to exceed an empirical detection threshold (STS: $3.3\,\mu m^2 cm^{-3}$, NAT: $0.25\,\mu m^2 cm^{-3}$, ice: $0.5\,\mu m^2 cm^{-3}$). The mixed type is chosen such that the simulated surface areas for both, STS and NAT, need to be beyond the threshold. The spatial patterns of ice PSC occurrence between MIPAS and CLaMS agrees very well (Fig. 4). The model simulates ice PSCs above Spitsbergen and in the center of the cold pool above the Russian Arctic. These are the same locations where MIPAS observed ice. NAT observations downstream of ice PSCs are also reproduced by the model. However, CLaMS produces more NAT PSCs over the North Pole than observed by MIPAS. A possible explanation for this discrepancy lies in the detection threshold of MIPAS. MIPAS may classify a volume of air as STS even though NAT particles are present with volume densities smaller than about $0.3\,\mu m^3 cm^{-3}$ or NAT particles with radii larger than $3\,\mu m$ (Höpfner et al., 2006a, b; Spang et al., 2018). Moreover, NAT clouds are mixtures of NAT and STS or even NAT, STS, and ice particles as emphasized by e.g. Peter and Grooß (2012) and Pitts et al. (2013, 2018) leading to the conclusion that the discrepancy between NAT and STS as seen in Fig. 4 might be a caveat in the MIPAS classification. However, as seen in the results for the Antarctic winter 2011, CLaMS also tends to overestimate NAT occurrences (compare Sect. 4.2).

Figure 5 demonstrates the effect of PSCs on the distribution of gas-phase HNO_3 and H_2O of the polar winter stratosphere. First, PSCs lead to a temporary removal of HNO_3 and H_2O from the gas phase by condensation onto NAT and ice particles, respectively, and uptake by STS droplets. In case of sedimentation, a permanent redistribution of the gas phase components takes place. The temporal evolution of Arctic H_2O is presented in Fig. 5 as function of potential temperature and time for the average vortex core (equivalent latitude $> 70°$ N). It shows predominantly the dynamically forced diabatic descent of air inside the polar vortex (compare Fig. 5, upper panels). Areas of low H_2O mixing ratios due to ice PSCs are too limited in the Arctic to be clearly seen in a vortex average. A tiny sign of water uptake by PSCs is visible mid of January at approximately 500 K in the MLS data. This effect is even smaller in the model simulation. In contrast, the patter of HNO_3 shows a clear layer of denitrified air in both, observations and simulations, at the end of December 2009 (compare Fig. 5, lower panels). Additionally, a layer of renitrified air forms between approximately 400 and 450 K. The redistribution of NO_y in the Arctic has already been shown but not compared to MLS observations by Grooß et al. (2014). The effect of the MLS averaging kernels turns out to be small in the Arctic winter 2009/2010 (compare Fig. 5, right column). Model results slightly converge towards the observations.

4.2 2011 Antarctic winter: comparison with observations

Figures 6 - 10 show the results for the Antarctic winter 2011 corresponding to the figures above shown for the Arctic winter 2009/2010. In addition, we present a number of days throughout the winter to demonstrate the evolution of PSCs and corresponding model simulations (Figs. 7, 8, and 9). Figure 6 shows the daily, height resolved values of PSC areal coverage and gives an overview of the PSC season in the SH 2011. Starting in the second half of May, CLaMS and CALIOP agree well with both showing NAT PSCs to be the first type of PSCs present in the season. In contrast, the MIPAS classifier detects STS clouds first. NAT PSCs follow some few days later due to data gaps. As already highlighted in the paragraph above, NAT clouds are

© Author(s) 2018. CC BY 4.0 License.

mixtures of NAT and STS particles and MIPAS will misclassify NAT particles with radii larger than 3 µm. Here, Fig. 8 shows a predominantly NAT cloud seen by CALIOP on 25 May whereas Fig. 9 shows STS droplets classified by MIPAS for the entire day. Size distributions from CLaMS simulations on 25 May 2011 point in the same direction, namely that simulated NAT number densities do not exceed $10^{-2}\,\mathrm{cm}^{-3}$ with particle radii larger than 5 µm (not shown). Going further in time, a large fraction of the vortex is covered by ice PSCs, typical for Antarctic winters. Also here, the agreement between CALIOP, MIPAS, and CLaMS is satisfying at PSC altitudes (Fig. 6). High values of NAT coverages seen in the MIPAS data at altitudes below 15 km can again be attributed to a bias in the PSC detection (Spang et al., 2018). Throughout the PSC season, we also looked at single clouds (Fig. 7 and Fig. 8) on individual days (Fig. 9) in detail. Discrepancies between both satellite datasets appear to be related to the relative proportion of STS and NAT PSCs with CLaMS overestimating NAT occurrences. Fig. 7 shows one such example where CLaMS produces widespread NAT particles in a region where CALIOP observes few NAT particles, possibly due to denitrification. Moreover, CLaMS simulations somewhat underestimate ice occurrences (e.g. Fig. 8, July and August). Nevertheless, the general seasonal evolution with variations in dominating PSC types, vertical PSC occurrences and spatial patterns is reproduced by the simulations.

The temporal evolution of gas-phase water vapor and nitric acid as measured by MLS and simulated by CLaMS is presented in Fig. 10. Dehydrated and denitrified areas are clearly seen in the MLS measurements and in the CLaMS simulations. Water vapor mixing ratios as low as 1.6 ppm (vortex core average) are observed. HNO_3 mixing ratios in the vortex core are extremely low and reach values of 200 ppt. Evaporation of sedimenting PSC particles produces layers of enriched H_2O (rehydrated) and HNO_3 (renitrified) air. They appear below the depleted regions as seen in both MLS observations and CLaMS. The results highlight the new capability of CLaMS to simulate the vertical redistribution of H_2O in good agreement with observations. The cirrus module of CLaMS would irreversibly remove the water in the dehydrated areas. In contrast, the new sedimentation module conserves H_2O. The signal of sedimentation with subsequent rehydration below is visible until the end of July in the observations as well as in the simulations. Thereafter, a diabatic descent of the rehydrated layer causes that water sedimenting from higher latitudes accumulates in the tropopause region. Vertical velocities are given by ERA-Interim diabatic heating rates. In October and November 2011, ERA-Interim holds already positive ascent rates and therefore cause the behavior seen in the simulations in spring. The temporal evolution of both species agrees very well between MLS and CLaMS. The total magnitude of dehydration is slightly smaller in the simulations than in the observations, which agrees with the impression that CLaMS simulations produce less ice than observed. The minimum values of HNO_3 compare very well but the vertical extent of the denitrified area in CLaMS could reach down to lower altitudes. Again, this agrees with the observations from PSC comparisons namely that NAT particles are present in the simulation but in combinations of number densities and sizes, which still have the potential to even better denitrify the stratosphere. Making use of the MLS averaging kernel smears out the eye-catching high values of HNO_3 at 650 K (compare Fig. 10, lower middle and right panel).

© Author(s) 2018. CC BY 4.0 License.

5 Conclusions

We present CLaMS simulations based on a new Lagrangian ice sedimentation scheme for the 2009/2010 Arctic and 2011 Antarctic winters. Previous CLaMS studies solely focused on the simulation of NAT PSCs and the corresponding denitrification. Here, we have extended the model by adding ice PSC particle nucleation, growth, sedimentation, and evaporation. Heterogeneous and homogeneous ice nucleation is included as well as NAT nucleation on preexisting ice particles. Heterogeneous ice nucleation rates are based on Engel et al. (2013), homogeneous ice nucleation occurs if the temperature exceeds a critical supersaturation (Kärcher and Lohmann, 2002). In addition, the implementation of ice particle nucleation requires the existence of small-scale temperature fluctuations (Gary, 2006, 2008) to be added to the synoptic-scale temperatures by ERA-Interim.

The agreement between CLaMS simulations and the CALIOP, MIPAS, and MLS observations on different temporal and spatial scales is convincing. CLaMS PSC areal coverage presented for both seasons is in good agreement between MIPAS, CALIOP, and CLaMS. Similar comparisons between satellite observations and model simulations have been performed in the past (e.g. Khosrawi et al., 2017, 2018; Zhu et al., 2017b, a). However, this is to our knowledge the first study presenting ample results of individual PSCs simulated by a global model in comparison to high resolution satellite observations. These detailed comparisons are also in agreement, but reveal some discrepancies. In general, CLaMS tends to overestimate NAT PSCs. In comparison to MIPAS, CLaMS simulates NAT particles at locations where MIPAS observes liquid PSC particles. At the onset of Antarctic PSC occurrence in May, CLaMS is in agreement with CALIOP that NAT clouds were first observed. MIPAS first observes STS, but is not sensitive to the presence of larger NAT particles (Höpfner et al., 2006a, b; Spang et al., 2018). However, the comparisons with CALIOP also shows differences in NAT occurrence. Cloud free areas, next to or surrounded by PSCs in the CALIOP data, are often populated with NAT particles in the CLaMS simulations. Looking at the temporal and vortex averaged evolution of HNO_3, denitrification in the SH simulation should reach down to lower altitudes. These findings point to shortcomings in the simulation of NAT particle sizes in combination with number densities namely that NAT particle sedimentation should be more efficient. Simulated ice PSCs, in turn, reveal a coverage slightly smaller than observed as seen in the comparison between CALIOP and CLaMS in the SH. CLaMS simulations miss wave ice clouds as seen in the beginning of the 2009/2010 Arctic winter, likely because ERA-Interim temperature fields are too coarse to resolve the required low values. The small-scale fluctuations added in this study are ubiquitous and not related to specific gravity wave sources such as mountains. The modeled extent of the dehydration signal fits with the H_2O observations, however, the level of dehydration in CLaMS should be larger, to lower the minimum values of H_2O in the simulations by about 0.5 ppm. So far, ice nucleation on preexisting NAT particles has not been considered in our CLaMS simulations. Recently, Voigt et al. (2017) speculated about the existence of this specific pathway, which was mentioned in the literature already two decades ago (e.g. Peter, 1997). Discussions about the importance of ice nucleation on NAT particles, e.g. for denitrification, are controversial (Khosrawi et al., 2011; Engel et al., 2014) and this topic may be a focus of future CLaMS studies.

© Author(s) 2018. CC BY 4.0 License.

Despite deficiencies, the overall agreement between CLaMS and different PSC and trace gas measurements is convincing. The advanced microphysical PSC scheme, which includes now STS, NAT, and ice PSCs, therefore represents a major improvement of the representation of cloud physics in CLaMS. Further studies will benefit from this development and may provide more insights into occurrence and importance of PSC types and their formation mechanisms.

Code and data availability. CLaMS code/data is available on request by the first author. Observational datasets from CALIOP, MIPAS, and MLS can be found on the following web pages (last accessed in March 2018):
MIPAS/Envisat Observations of PSCs: https://datapub.fz-juelich.de/slcs/mipas/psc/
CALIPSO/CALIOP L2 PSC Mask (v1): https://doi.org/10.5067/caliop/calipso/lid_l1-standard-v4-10
Aura MLS H_2O product: https://mls.jpl.nasa.gov/products/h2o_product.php
Aura MLS HNO_3 product: https://mls.jpl.nasa.gov/products/hno3_product.php

Competing interests. The authors declare that they have no conflict of interest.

Acknowledgements. We thank Beiping P. Luo for sharing his Mie and T-Matrix calculations with us. We also thank Felix Ploeger and Paul Konopka for providing the data of the multi-annual CLaMS simulation. Nicole Thomas gave excellent support for our programming activities. We gratefully acknowledge the European Centre for Medium-Range Weather Forecasts (ECMWF) for providing ERA-Interim data. We thank Michelle Santee and the MLS team for providing their high quality data sets. Computing time has been granted on the supercomputer JURECA at the Jülich Supercomputing Centre (JSC) under the VSR project ID JICG11. Ines Tritscher was funded by the Deutsche Forschungsgemeinschaft (DFG) under project number 310479827. We finally acknowledge the Stratosphere-troposphere Processes And their Role in Climate (SPARC) project and the International Space Science Institute (ISSI) for supporting the Polar Stratospheric Cloud Initiative (PSCi).

© Author(s) 2018. CC BY 4.0 License.

References

Alexander, S. P., Klekociuk, A. R., Pitts, M. C., McDonald, A. J., and Arevalo-Torres, A.: The effect of orographic gravity waves on Antarctic polar stratospheric cloud occurrence and composition, J. Geophys. Res. A, 116, https://doi.org/10.1029/2010JD015184, d06109, 2011.

Biermann, U. M., Crowley, J. N., Huthwelker, T., Moortgat, G. K., Crutzen, P. J., and Peter, T.: FTIR studies on lifetime prolongation of stratospheric ice particles due to NAT coating, Geophys. Res. Lett., 25, 3939–3942, 1998.

Carslaw, K. S., Wirth, M., Tsias, A., Luo, B. P., Dörnbrack, A., Leutbecher, M., Volkert, H., Renger, W., Bacmeister, J. T., and Peter, T.: Particle microphysics and chemistry in remotely observed mountain polar stratospheric clouds, J. Geophys. Res., 103, 5785–5796, https://doi.org/10.1029/97JD03626, 1998a.

Carslaw, K. S., Wirth, M., Tsias, A., Luo, B. P., Dörnbrack, A., Leutbecher, M., Volkert, H., Renger, W., Bacmeister, J. T., Reimer, E., and Peter, T.: Increased stratospheric ozone depletion due to mountain-induced atmospheric waves, Nature, 391, 675–678, https://doi.org/10.1038/35589, 1998b.

Carslaw, K. S., Kettleborough, J. A., Northway, M. J., Davies, S., Gao, R.-S., Fahey, D. W., Baumgardner, D. G., Chipperfield, M. P., and Kleinböhl, A.: A vortex-scale simulation of the growth and sedimentation of large nitric acid hydrate particles, J. Geophys. Res. A, 107, SOL 43–1–SOL 43–16, https://doi.org/10.1029/2001JD000467, 8300, 2002.

Carslaw, K. S., Luo, B. P., Clegg, S. L., Peter, T., Brimblecombe, P., and Crutzen, P. J.: Stratospheric aerosol growth and HNO_3 gas phase depletion from coupled HNO_3 and water uptake by liquid particles, Geophys. Res. Lett., 21, 2479–2482, 1994.

Daerden, F., Larsen, N., Chabrillat, S., Errera, Q., Bonjean, S., Fonteyn, D., Hoppel, K., and Fromm, M.: A 3D-CTM with detailed online PSC-microphysics: analysis of the Antarctic winter 2003 by comparison with satellite observations, Atmos. Chem. Phys., 7, 1755–1772, https://doi.org/10.5194/acp-7-1755-2007, 2007.

Dee, D. P., Uppala, S. M., Simmons, A. J., Berrisford, P., Poli, P., Kobayashi, S., Andrae, U., Balmaseda, M. A., Balsamo, G., Bauer, P., Bechtold, P., Beljaars, A. C. M., van de Berg, L., Bidlot, J., Bormann, N., Delsol, C., Dragani, R., Fuentes, M., Geer, A. J., Haimberger, L., Healy, S. B., Hersbach, H., Hólm, E. V., Isaksen, L., Kållberg, P., Köhler, M., Matricardi, M., McNally, A. P., Monge-Sanz, B. M., Morcrette, J.-J., Park, B.-K., Peubey, C., de Rosnay, P., Tavolato, C., Thépaut, J.-N., and Vitart, F.: The ERA-Interim reanalysis: configuration and performance of the data assimilation system, Q. J. R. Meteorol. Soc., 137, 553–597, https://doi.org/10.1002/qj.828, 2011.

Dörnbrack, A., Birner, T., Fix, A., Flentje, H., Meister, A., Schmid, H., Browell, E. V., and Mahoney, M. J.: Evidence for inertia gravity waves forming polar stratospheric clouds over Scandinavia, J. Geophys. Res. A, 107, SOL 30–1–SOL 30–18, https://doi.org/10.1029/2001JD000452, 8287, 2002.

Drdla, K. and Müller, R.: Temperature thresholds for chlorine activation and ozone loss in the polar stratosphere, Ann. Geophys., 30, 1055–1073, https://doi.org/10.5194/angeo-30-1055-2012, 2012.

Engel, I., Luo, B. P., Pitts, M. C., Poole, L. R., Hoyle, C. R., Grooß, J.-U., Dörnbrack, A., and Peter, T.: Heterogeneous formation of polar stratospheric clouds – Part 2: Nucleation of ice on synoptic scales, Atmos. Chem. Phys., 13, 10 769–10 785, https://doi.org/10.5194/acp-13-10769-2013, 2013.

Engel, I., Luo, B. P., Khaykin, S. M., Wienhold, F. G., Vömel, H., Kivi, R., Hoyle, C. R., Grooß, J.-U., Pitts, M. C., and Peter, T.: Arctic stratospheric dehydration – Part 2: Microphysical modeling, Atmos. Chem. Phys., 14, 3231–3246, https://doi.org/10.5194/acp-14-3231-2014, 2014.

Fahey, D. W., Gao, R. S., Carslaw, K. S., Kettleborough, J., Popp, P. J., Northway, M. J., Holecek, J. C., Ciciora, S. C., McLaughlin, R. J., Thompson, T. L., Winkler, R. H., Baumgardner, D. G., Gandrud, B., Wennberg, P. O., Dhaniyala, S., McKinney, K., Pe-

© Author(s) 2018. CC BY 4.0 License.

ter, T., Salawitch, R. J., Bui, T. P., Elkins, J. W., Webster, C. R., Atlas, E. L., Jost, H., Wilson, J. C., Herman, R. L., Kleinböhl, A., and von König, M.: The Detection of Large HNO3-Containing Particles in the Winter Arctic Stratosphere, Science, 291, 1026–1031, https://doi.org/10.1126/science.1057265, 2001.

Fischer, H., Birk, M., Blom, C., Carli, B., Carlotti, M., von Clarmann, T., Delbouille, L., Dudhia, A., Ehhalt, D., Endemann, M., Flaud, J. M., Gessner, R., Kleinert, A., Koopman, R., Langen, J., López-Puertas, M., Mosner, P., Nett, H., Oelhaf, H., Perron, G., Remedios, J., Ridolfi, M., Stiller, G., and Zander, R.: MIPAS: an instrument for atmospheric and climate research, Atmos. Chem. Phys., 8, 2151–2188, https://doi.org/10.5194/acp-8-2151-2008, 2008.

Fueglistaler, S., Buss, S., Luo, B. P., Wernli, H., Flentje, H., Hostetler, C. A., Poole, L. R., Carslaw, K. S., and Peter, T.: Detailed modeling of mountain wave PSCs, Atmos. Chem. Phys., 3, 697–712, https://doi.org/10.5194/acp-3-697-2003, 2003.

Gary, B. L.: Mesoscale temperature fluctuations in the stratosphere, Atmos. Chem. Phys., 6, 4577–4589, https://doi.org/10.5194/acp-6-4577-2006, 2006.

Gary, B. L.: Mesoscale temperature fluctuations in the Southern Hemisphere stratosphere, Atmos. Chem. Phys., 8, 4677–4681, 2008.

Grooß, J.-U., Günther, G., Müller, R., Konopka, P., Bausch, S., Schlager, H., Voigt, C., Volk, C. M., and Toon, G. C.: Simulation of denitrification and ozone loss for the Arctic winter 2002/2003, Atmos. Chem. Phys., 5, 1437–1448, https://doi.org/10.5194/acp-5-1437-2005, 2005.

Grooß, J.-U., Engel, I., Borrmann, S., Frey, W., Günther, G., Hoyle, C. R., Kivi, R., Luo, B. P., Molleker, S., Peter, T., Pitts, M. C., Schlager, H., Stiller, G., Vömel, H., Walker, K. A., and Müller, R.: Nitric acid trihydrate nucleation and denitrification in the Arctic stratosphere, Atmos. Chem. Phys., 14, 1055–1073, https://doi.org/10.5194/acp-14-1055-2014, 2014.

Grooß, J.-U., Müller, R., Spang, R., Tritscher, I., Wegner, T., Chipperfield, M. P., Feng, W., Kinnison, D. E., and Madronich, S.: On the discrepancy of HCl processing in the dark polar vortices, Atmos. Chem. Phys. Discuss., pp. 1–28, https://doi.org/10.5194/acp-2018-202, 2018.

Hanson, D. and Mauersberger, K.: Laboratory studies of the nitric acid trihydrate: Implications for the south polar stratosphere, Geophys. Res. Lett., 15, 855–858, https://doi.org/10.1029/GL015i008p00855, 1988.

Hoffmann, L., Spang, R., Orr, A., Alexander, M. J., Holt, L. A., and Stein, O.: A decadal satellite record of gravity wave activity in the lower stratosphere to study polar stratospheric cloud formation, Atmos. Chem. Phys., 17, 2901–2920, https://doi.org/10.5194/acp-17-2901-2017, 2017.

Höpfner, M., Larsen, N., Spang, R., Luo, B. P., Ma, J., Svendsen, S. H., Eckermann, S. D., Knudsen, B., Massoli, P., Cairo, F., Stiller, G., v. Clarmann, T., and Fischer, H.: MIPAS detects Antarctic stratospheric belt of NAT PSCs caused by mountain waves, Atmos. Chem. Phys., 6, 1221–1230, https://doi.org/10.5194/acp-6-1221-2006, 2006a.

Höpfner, M., Luo, B. P., Massoli, P., Cairo, F., Spang, R., Snels, M., Di Donfrancesco, G., Stiller, G., von Clarmann, T., Fischer, H., and Biermann, U.: Spectroscopic evidence for NAT, STS, and ice in MIPAS infrared limb emission measurements of polar stratospheric clouds, Atmos. Chem. Phys., 6, 1201–1219, https://doi.org/10.5194/acp-6-1201-2006, 2006b.

Hoyle, C. R., Engel, I., Luo, B. P., Pitts, M. C., Poole, L. R., Grooß, J.-U., and Peter, T.: Heterogeneous formation of polar stratospheric clouds – Part 1: Nucleation of nitric acid trihydrate (NAT), Atmos. Chem. Phys., 13, 9577–9595, https://doi.org/10.5194/acp-13-9577-2013, 2013.

Hoyle, C. R., Luo, B. P., and Peter, T.: The origin of high ice crystal number densities in cirrus clouds, J. Atmos. Sci., 62, 2568–2579, https://doi.org/10.1175/JAS3487.1, 2005.

© Author(s) 2018. CC BY 4.0 License.

Kärcher, B. and Lohmann, U.: A parameterization of cirrus cloud formation: Homogeneous freezing of supercooled aerosols, J. Geophys. Res., 107, AAC 4–1–AAC 4–10, https://doi.org/10.1029/2001JD000470, 2002.

Kärcher, B., Dörnbrack, A., and Sölch, I.: Supersaturation Variability and Cirrus Ice Crystal Size Distributions, J. Atmos. Sci., 71, 2905–2926, https://doi.org/10.1175/JAS-D-13-0404.1, 2014.

Kelly, K. K., Tuck, A. F., Murphy, D. M., Proffitt, M. H., Fahey, D. W., Jones, R. L., McKenna, D. S., Loewenstein, M., Podolske, J. R., Strahan, S. E., Ferry, G. V., Chan, K. R., Vedder, J. F., Gregory, G. L., Hypes, W. D., McCormick, M. P., Browell, E. V., and Heidt, L. E.: Dehydration in the lower Antarctic stratosphere during late winter and early spring, 1987, J. Geophys. Res., 94, 11 317–11 357, https://doi.org/10.1029/JD094iD09p11317, 1989.

Khosrawi, F., Urban, J., Pitts, M. C., Voelger, P., Achtert, P., Kaphlanov, M., Santee, M. L., Manney, G. L., Murtagh, D., and Fricke, K.-H.: Denitrification and polar stratospheric cloud formation during the Arctic winter 2009/2010, Atmos. Chem. Phys., 11, 8471–8487, https://doi.org/10.5194/acp-11-8471-2011, 2011.

Khosrawi, F., Kirner, O., Sinnhuber, B.-M., Johansson, S., Höpfner, M., Santee, M. L., Froidevaux, L., Ungermann, J., Ruhnke, R., Woiwode, W., Oelhaf, H., and Braesicke, P.: Denitrification, dehydration and ozone loss during the 2015/2016 Arctic winter, Atmos. Chem. Phys., 17, 12 893–12 910, https://doi.org/10.5194/acp-17-12893-2017, 2017.

Khosrawi, F., Kirner, O., Stiller, G., Höpfner, M., Santee, M. L., Kellmann, S., and Braesicke, P.: Comparison of ECHAM5/MESSy Atmospheric Chemistry (EMAC) Simulations of the Arctic winter 2009/2010 and 2010/2011 with Envisat/MIPAS and Aura/MLS Observations, Atmos. Chem. Phys. Discuss., 2018, 1–31, https://doi.org/10.5194/acp-2017-1190, 2018.

Kirner, O., Ruhnke, R., Buchholz-Dietsch, J., Jöckel, P., Brühl, C., and Steil, B.: Simulation of polar stratospheric clouds in the chemistry-climate-model EMAC via the submodel PSC, Geosci. Model Dev., 4, 169–182, https://doi.org/10.5194/gmd-4-169-2011, 2011.

Kirner, O., Müller, R., Ruhnke, R., and Fischer, H.: Contribution of liquid, NAT and ice particles to chlorine activation and ozone depletion in Antarctic winter and spring, Atmos. Chem. Phys., 15, 2019–2030, https://doi.org/10.5194/acp-15-2019-2015, 2015.

Klekociuk, A. R., Tully, M. B., Krummel, P. B., Gies, H. P., Petelina, S. V., Alexander, S. P., Deschamps, L. L., Fraser, P. J., Henderson, S. I., Javorniczky, J., Shanklin, J. D., Siddaway, J. M., and Stone, K. A.: The Antarctic ozone hole during 2011, Aust. Meteorol. Oceanogr. J., 64, 293–311, 2014.

Konopka, P., Steinhorst, H.-M., Grooß, J.-U., Günther, G., Müller, R., Elkins, J. W., Jost, H.-J., Richard, E., Schmidt, U., Toon, G., and McKenna, D. S.: Mixing and ozone loss in the 1999–2000 Arctic vortex: Simulations with the three-dimensional Chemical Lagrangian Model of the Stratosphere (CLaMS), J. Geophys. Res., 109, D02315, https://doi.org/10.1029/2003JD003792, d02315, 2004.

Koop, T., Luo, B. P., Tsias, A., and Peter, T.: Water activity as the determinant for homogeneous ice nucleation in aqueous solutions, Nature, 406, 611–614, https://doi.org/10.1038/35020537, 2000.

Krämer, M., Schiller, C., Afchine, A., Bauer, R., Gensch, I., Mangold, A., Schlicht, S., Spelten, N., Sitnikov, N., Borrmann, S., de Reus, M., and Spichtinger, P.: Ice supersaturations and cirrus cloud crystal numbers, Atmos. Chem. Phys., 9, 3505–3522, https://doi.org/10.5194/acp-9-3505-2009, 2009.

Livesey, N. J., Read, W. G., Wagner, P. A., Froidevaux, L., Lambert, A., Manney, G. L., Valle, L. F. M., Pumphrey, H. C., Santee, M. L., Schwartz, M. J., Wang, S., Fuller, R. A., Jarnot, R. F., Knosp, B. W., and Martinez, E.: Version 4.2x Level 2 data quality and description document, Tech. Rep. JPL D-33509 Rev. C, Jet Propulsion Laboratory, http://mls.jpl.nasa.gov, 2017.

Luo, B. P., Voigt, C., Fueglistaler, S., and Peter, T.: Extreme NAT supersaturations in mountain wave ice PSCs: A clue to NAT formation, J. Geophys. Res., 108, 4441, https://doi.org/10.1029/2002JD003104, 2003.

© Author(s) 2018. CC BY 4.0 License.

Manney, G. L. and Lawrence, Z. D.: The major stratospheric final warming in 2016: dispersal of vortex air and termination of Arctic chemical ozone loss, Atmos. Chem. Phys., 16, 15 371–15 396, https://doi.org/10.5194/acp-16-15371-2016, 2016.

Marcolli, C., Gedamke, S., Peter, T., and Zobrist, B.: Efficiency of immersion mode ice nucleation on surrogates of mineral dust, Atmos. Chem. Phys., 7, 5081–5091, https://doi.org/10.5194/acp-7-5081-2007, 2007.

Maturilli, M. and Dörnbrack, A.: Polar stratospheric ice cloud above Spitsbergen, J. Geophys. Res., 111, D18210, https://doi.org/10.1029/2005JD006967, 2006.

McKenna, D. S., Grooß, J.-U., Günther, G., Konopka, P., Müller, R., Carver, G., and Sasano, Y.: A new Chemical Lagrangian Model of the Stratosphere (CLaMS) 2. Formulation of chemistry scheme and initialization, J. Geophys. Res., 107, 4256, https://doi.org/10.1029/2000JD000113, 2002a.

McKenna, D. S., Konopka, P., Grooß, J.-U., Günther, G., Müller, R., Spang, R., Offermann, D., and Orsolini, Y.: A new Chemical Lagrangian Model of the Stratosphere (CLaMS) - 1. Formulation of advection and mixing, J. Geophys. Res., 107, 4309, https://doi.org/10.1029/2000JD000114, 2002b.

Meilinger, S. K., Koop, T., Luo, B. P., Huthwelker, T., Carslaw, K. S., Krieger, U., Crutzen, P. J., and Peter, T.: Size-dependent stratospheric droplet composition in lee wave temperature fluctuations and their potential role in PSC freezing, Geophys. Res. Lett., 22, 3031–3034, https://doi.org/10.1029/95GL03056, 1995.

Mishchenko, M. I., Travis, L. D., and Mackowski, D. W.: T-Matrix Computations of Light Scattering by Nonspherical Particles: A Review (Reprinted from vol 55, pg 535-575, 1996), J. Quant. Spectrosc. Radiat. Transf., 111, 1704–1744, https://doi.org/10.1016/0022-4073(96)00002-7, 2010.

Molleker, S., Borrmann, S., Schlager, H., Luo, B., Frey, W., Klingebiel, M., Weigel, R., Ebert, M., Mitev, V., Matthey, R., Woiwode, W., Oelhaf, H., Dörnbrack, A., Stratmann, G., Grooß, J.-U., Günther, G., Vogel, B., Müller, R., Krämer, M., Meyer, J., and Cairo, F.: Microphysical properties of synoptic-scale polar stratospheric clouds: in situ measurements of unexpectedly large HNO_3-containing particles in the Arctic vortex, Atmos. Chem. Phys., 14, 10 785–10 801, https://doi.org/10.5194/acp-14-10785-2014, 2014.

Morgenstern, O., Hegglin, M. I., Rozanov, E., O'Connor, F. M., Abraham, N. L., Akiyoshi, H., Archibald, A. T., Bekki, S., Butchart, N., Chipperfield, M. P., Deushi, M., Dhomse, S. S., Garcia, R. R., Hardiman, S. C., Horowitz, L. W., Jöckel, P., Josse, B., Kinnison, D., Lin, M., Mancini, E., Manyin, M. E., Marchand, M., Marécal, V., Michou, M., Oman, L. D., Pitari, G., Plummer, D. A., Revell, L. E., Saint-Martin, D., Schofield, R., Stenke, A., Stone, K., Sudo, K., Tanaka, T. Y., Tilmes, S., Yamashita, Y., Yoshida, K., and Zeng, G.: Review of the global models used within phase 1 of the Chemistry–Climate Model Initiative (CCMI), Geosci. Model Dev., 10, 639–671, https://doi.org/10.5194/gmd-10-639-2017, 2017.

Murphy, D. M. and Koop, T.: Review of the vapour pressures of ice and supercooled water for atmospheric applications, Q. J. R. Meteorol. Soc., 131, 1539–1565, https://doi.org/10.1256/qj.04.94, 2005.

Noel, V. and Pitts, M.: Gravity wave events from mesoscale simulations, compared to polar stratospheric clouds observed from spaceborne lidar over the Antarctic Peninsula, J. Geophys. Res. A, 117, D11207, https://doi.org/10.1029/2011JD017318, 2012.

Orr, A., Hosking, J. S., Hoffmann, L., Keeble, J., Dean, S. M., Roscoe, H. K., Abraham, N. L., Vosper, S., and Braesicke, P.: Inclusion of mountain-wave-induced cooling for the formation of PSCs over the Antarctic Peninsula in a chemistry–climate model, Atmos. Chem. Phys., 15, 1071–1086, https://doi.org/10.5194/acp-15-1071-2015, 2015.

Peter, T.: Microphysics and heterogeneous chemistry of polar stratospheric clouds, Ann. Rev. Phys. Chem., 48, 785–822, 1997.

© Author(s) 2018. CC BY 4.0 License.

Peter, T. and Grooß, J.-U.: Chapter 4: Polar Stratospheric Clouds and Sulfate Aerosol Particles: Microphysics, Denitrification and Heterogeneous Chemistry, in: Stratospheric Ozone Depletion and Climate Change, pp. 108–144, The Royal Society of Chemistry, https://doi.org/10.1039/9781849733182-00108, 2012.

Pitts, M. C., Poole, L. R., Lambert, A., and Thomason, L. W.: An assessment of CALIOP polar stratospheric cloud composition classification, Atmos. Chem. Phys., 13, 2975–2988, https://doi.org/10.5194/acp-13-2975-2013, 2013.

Pitts, M. C., Poole, L. R., and Gonzalez, R.: Polar stratospheric cloud climatology based on CALIPSO spaceborne lidar measurements from 2006–2017, Atmos. Chem. Phys. Discuss., 2018, 1–54, https://doi.org/10.5194/acp-2018-234, 2018.

Pitts, M. C., Poole, L. R., Dörnbrack, A., and Thomason, L. W.: The 2009-2010 Arctic polar stratospheric cloud season: a CALIPSO perspective, Atmos. Chem. Phys., 11, 2161–2177, https://doi.org/0.5194/acp-11-2161-2011, 2011.

Ploeger, F., Konopka, P., Günther, G., Grooß, J.-U., and Müller, R.: Impact of the vertical velocity scheme on modeling transport in the tropical tropopause layer, J. Geophys. Res., 115, D03301, https://doi.org/10.1029/2009JD012023, 2010.

Ploeger, F., Günther, G., Konopka, P., Fueglistaler, S., Müller, R., Hoppe, C., Kunz, A., Spang, R., Grooß, J.-U., and Riese, M.: Horizontal water vapor transport in the lower stratosphere from subtropics to high latitudes during boreal summer, J. Geophys. Res., 118, 8111–8127, https://doi.org/10.1002/jgrd.50636, 2013.

Podglajen, A., Hertzog, A., Plougonven, R., and Legras, B.: Lagrangian temperature and vertical velocity fluctuations due to gravity waves in the lower stratosphere, Geophys. Res. Lett., 43, 3543–3553, https://doi.org/10.1002/2016GL068148, 2016GL068148, 2016.

Pommrich, R., Müller, R., Grooß, J.-U., Konopka, P., Ploeger, F., Vogel, B., Tao, M., Hoppe, C. M., Günther, G., Spelten, N., Hoffmann, L., Pumphrey, H.-C., Viciani, S., D'Amato, F., Volk, C. M., Hoor, P., Schlager, H., and Riese, M.: Tropical troposphere to stratosphere transport of carbon monoxide and long-lived trace species in the Chemical Lagrangian Model of the Stratosphere (CLaMS), Geosci. Model Dev., 7, 2895–2916, https://doi.org/10.5194/gmd-7-2895-2014, 2014.

Riese, M., Ploeger, F., Rap, A., Vogel, B., Konopka, P., Dameris, M., and Forster, P.: Impact of uncertainties in atmospheric mixing on simulated UTLS composition and related radiative effects, J. Geophys. Res. A, 117, D16305, https://doi.org/10.1029/2012JD017751, 2012.

Solomon, S.: Stratospheric ozone depletion: A review of concepts and history, Rev. Geophys., 37, 275–316, https://doi.org/10.1029/1999RG900008, 1999.

Solomon, S., Kinnison, D., Bandoro, J., and Garcia, R.: Simulation of polar ozone depletion: An update, J. Geophys. Res., 120, 7958–7974, https://doi.org/10.1002/2015JD023365, 2015.

Solomon, S., Ivy, D. J., Kinnison, D., Mills, M. J., Neely, R. R., and Schmidt, A.: Emergence of healing in the Antarctic ozone layer, Science, 353, 269–274, https://doi.org/10.1126/science.aae0061, 2016.

Solomon, S., Garcia, R. R., Rowland, F. S., and Wuebbles, D. J.: On the depletion of Antarctic ozone, Nature, 321, 755–758, 1986.

Spang, R. and Remedios, J. J.: Observations of a distinctive infra-red spectral feature in the atmospheric spectra of polar stratospheric clouds measured by the CRISTA instrument, Geophys. Res. Lett., 30, https://doi.org/10.1029/2003GL017231, 1875, 2003.

Spang, R., Arndt, K., Dudhia, A., Höpfner, M., Hoffmann, L., Hurley, J., Grainger, R. G., Griessbach, S., Poulsen, C., Remedios, J. J., Riese, M., Sembhi, H., Siddans, R., Waterfall, A., and Zehner, C.: Fast cloud parameter retrievals of MIPAS/Envisat, Atmos. Chem. Phys., 12, 7135–7164, https://doi.org/10.5194/acp-12-7135-2012, 2012.

Spang, R., Hoffmann, L., Höpfner, M., Griessbach, S., Müller, R., Pitts, M. C., Orr, A. M. W., and Riese, M.: A multi-wavelength classification method for polar stratospheric cloud types using infrared limb spectra, Atmos. Meas. Tech., 9, 3619–3639, https://doi.org/10.5194/amt-9-3619-2016, 2016.

© Author(s) 2018. CC BY 4.0 License.

Spang, R., Hoffmann, L., Müller, R., Grooß, J.-U., Tritscher, I., Höpfner, M., Pitts, M., Orr, A., and Riese, M.: A climatology of polar stratospheric cloud composition between 2002 and 2012 based on MIPAS/Envisat observations, Atmos. Chem. Phys., 18, 5089–5113, https://doi.org/10.5194/acp-18-5089-2018, 2018.

Stephens, G. L., Vane, D. G., Boain, R. J., Mace, G. G., Sassen, K., Wang, Z. E., Illingworth, A. J., O'Connor, E. J., Rossow, W. B., Durden, S. L., Miller, S. D., Austin, R. T., Benedetti, A., Mitrescu, C., and Team, C. S.: The cloudsat mission and the a-train - A new dimension of space-based observations of clouds and precipitation, Bull. Am. Meteorol. Soc., 83, 1771–1790, 2002.

Tabazadeh, A., Djikaev, Y. S., Hamill, P., and Reiss, H.: Laboratory Evidence for Surface Nucleation of Solid Polar Stratospheric Cloud Particles, J. Phys. Chem. A, 106, 10 238–10 246, https://doi.org/10.1021/jp021045k, 2002.

Voigt, C., Schlager, H., Luo, B. P., Dörnbrack, A., Roiger, A., Stock, P., Curtius, J., Vössing, H., Borrmann, S., Davies, S., Konopka, P., Schiller, C., Shur, G., and Peter, T.: Nitric Acid Trihydrate (NAT) formation at low NAT supersaturation in Polar Stratospheric Clouds (PSCs), Atmos. Chem. Phys., 5, 1371–1380, https://doi.org/10.5194/acp-5-1371-2005, 2005.

Voigt, C., Dörnbrack, A., Wirth, M., Groß, S. M., Pitts, M. C., Poole, L. R., Baumann, R., Ehard, B., Sinnhuber, B.-M., Woiwode, W., and Oelhaf, H.: Widespread polar stratospheric ice clouds in the 2015/2016 Arctic winter – Implications for ice nucleation, Atmos. Chem. Phys. Discuss., 2017, 1–29, https://doi.org/10.5194/acp-2017-1044, 2017.

von Hobe, M., Bekki, S., Borrmann, S., Cairo, F., D'Amato, F., Di Donfrancesco, G., Dörnbrack, A., Ebersoldt, A., Ebert, M., Emde, C., Engel, I., Ern, M., Frey, W., Genco, S., Griessbach, S., Grooß, J.-U., Gulde, T., Günther, G., Hösen, E., Hoffmann, L., Homonnai, V., Hoyle, C. R., Isaksen, I. S. A., Jackson, D. R., Jánosi, I. M., Jones, R. L., Kandler, K., Kalicinsky, C., Keil, A., Khaykin, S. M., Khosrawi, F., Kivi, R., Kuttippurath, J., Laube, J. C., Lefèvre, F., Lehmann, R., Ludmann, S., Luo, B. P., Marchand, M., Meyer, J., Mitev, V., Molleker, S., Müller, R., Oelhaf, H., Olschewski, F., Orsolini, Y., Peter, T., Pfeilsticker, K., Piesch, C., Pitts, M. C., Poole, L. R., Pope, F. D., Ravegnani, F., Rex, M., Riese, M., Röckmann, T., Rognerud, B., Roiger, A., Rolf, C., Santee, M. L., Scheibe, M., Schiller, C., Schlager, H., Siciliani de Cumis, M., Sitnikov, N., Søvde, O. A., Spang, R., Spelten, N., Stordal, F., Sumińska-Ebersoldt, O., Ulanovski, A., Ungermann, J., Viciani, S., Volk, C. M., vom Scheidt, M., von der Gathen, P., Walker, K., Wegner, T., Weigel, R., Weinbruch, S., Wetzel, G., Wienhold, F. G., Wohltmann, I., Woiwode, W., Young, I. A. K., Yushkov, V., Zobrist, B., and Stroh, F.: Reconciliation of essential process parameters for an enhanced predictability of Arctic stratospheric ozone loss and its climate interactions (RECONCILE): activities and results, Atmos. Chem. Phys., 13, 9233–9268, https://doi.org/10.5194/acp-13-9233-2013, 2013.

Waters, J. W., Froidevaux, L., Harwood, R. S., Jarnot, R. F., Pickett, H. M., Read, W. G., Siegel, P. H., Cofield, R. E., Filipiak, M. J., Flower, D. A., Holden, J. R., Lau, G. K. K., Livesey, N. J., Manney, G. L., Pumphrey, H. C., Santee, M. L., Wu, D. L., Cuddy, D. T., Lay, R. R., Loo, M. S., Perun, V. S., Schwartz, M. J., Stek, P. C., Thurstans, R. P., Boyles, M. A., Chandra, K. M., Chavez, M. C., Chen, G. S., Chudasama, B. V., Dodge, R., Fuller, R. A., Girard, M. A., Jiang, J. H., Jiang, Y. B., Knosp, B. W., LaBelle, R. C., Lam, J. C., Lee, K. A., Miller, D., Oswald, J. E., Patel, N. C., Pukala, D. M., Quintero, O., Scaff, D. M., Van Snyder, W., Tope, M. C., Wagner, P. A., and Walch, M. J.: The Earth Observing System Microwave Limb Sounder (EOS MLS) on the Aura satellite, IEEE Trans. Geosci. Remote Sensing, 44, 1075–1092, https://doi.org/10.1109/TGRS.2006.873771, 2006.

WMO: Scientific assessment of ozone depletion: 2014, Global Ozone Research and Monitoring Project–Report No. 55, Geneva, Switzerland, 2014.

Wohltmann, I., Wegner, T., Müller, R., Lehmann, R., Rex, M., Manney, G. L., Santee, M. L., Bernath, P., Sumińska-Ebersoldt, O., Stroh, F., von Hobe, M., Volk, C. M., Hösen, E., Ravegnani, F., Ulanovsky, A., and Yushkov, V.: Uncertainties in modelling heterogeneous chemistry and Arctic ozone depletion in the winter 2009/2010, Atmos. Chem. Phys., 13, 3909–3929, 2013.

© Author(s) 2018. CC BY 4.0 License.

Zhu, Y., Toon, O. B., Lambert, A., Kinnison, D. E., Brakebusch, M., Bardeen, C. G., Mills, M. J., and English, J. M.: Development of a Polar Stratospheric Cloud Model within the Community Earth System Model using constraints on Type I PSCs from the 2010–2011 Arctic winter, J. Adv. Model. Earth Syst., 7, 551–585, https://doi.org/10.1002/2015MS000427, 2015.

Zhu, Y., Toon, O. B., Lambert, A., Kinnison, D. E., Bardeen, C., and Pitts, M. C.: Development of a Polar Stratospheric Cloud Model Within the Community Earth System Model: Assessment of 2010 Antarctic Winter, J. Geophys. Res. A, 122, 10,418–10,438, https://doi.org/10.1002/2017JD027003, 2017JD027003, 2017a.

Zhu, Y., Toon, O. B., Pitts, M. C., Lambert, A., Bardeen, C., and Kinnison, D. E.: Comparing simulated PSC optical properties with CALIPSO observations during the 2010 Antarctic winter, J. Geophys. Res. A, 122, 1175–1202, https://doi.org/10.1002/2016JD025191, 2016JD025191, 2017b.

Atmos. Chem. Phys. Discuss., https://doi.org/10.5194/acp-2018-337
Manuscript under review for journal Atmos. Chem. Phys.
Discussion started: 15 May 2018
© Author(s) 2018. CC BY 4.0 License.

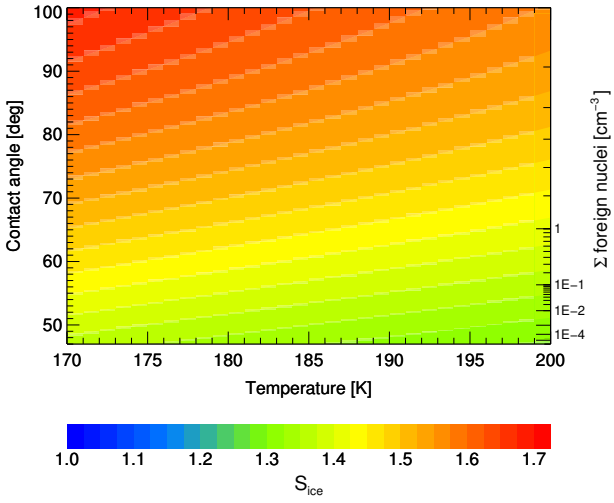

Figure 1. Visualization of the heterogeneous ice nucleation parameterization derived from Engel et al. (2013). The sum of foreign nuclei initiating heterogeneous ice nucleation (equal to a certain contact angle) resulting from a combination of temperature and supersaturation (color-coded).

Atmos. Chem. Phys. Discuss., https://doi.org/10.5194/acp-2018-337
Manuscript under review for journal Atmos. Chem. Phys.
Discussion started: 15 May 2018
© Author(s) 2018. CC BY 4.0 License.

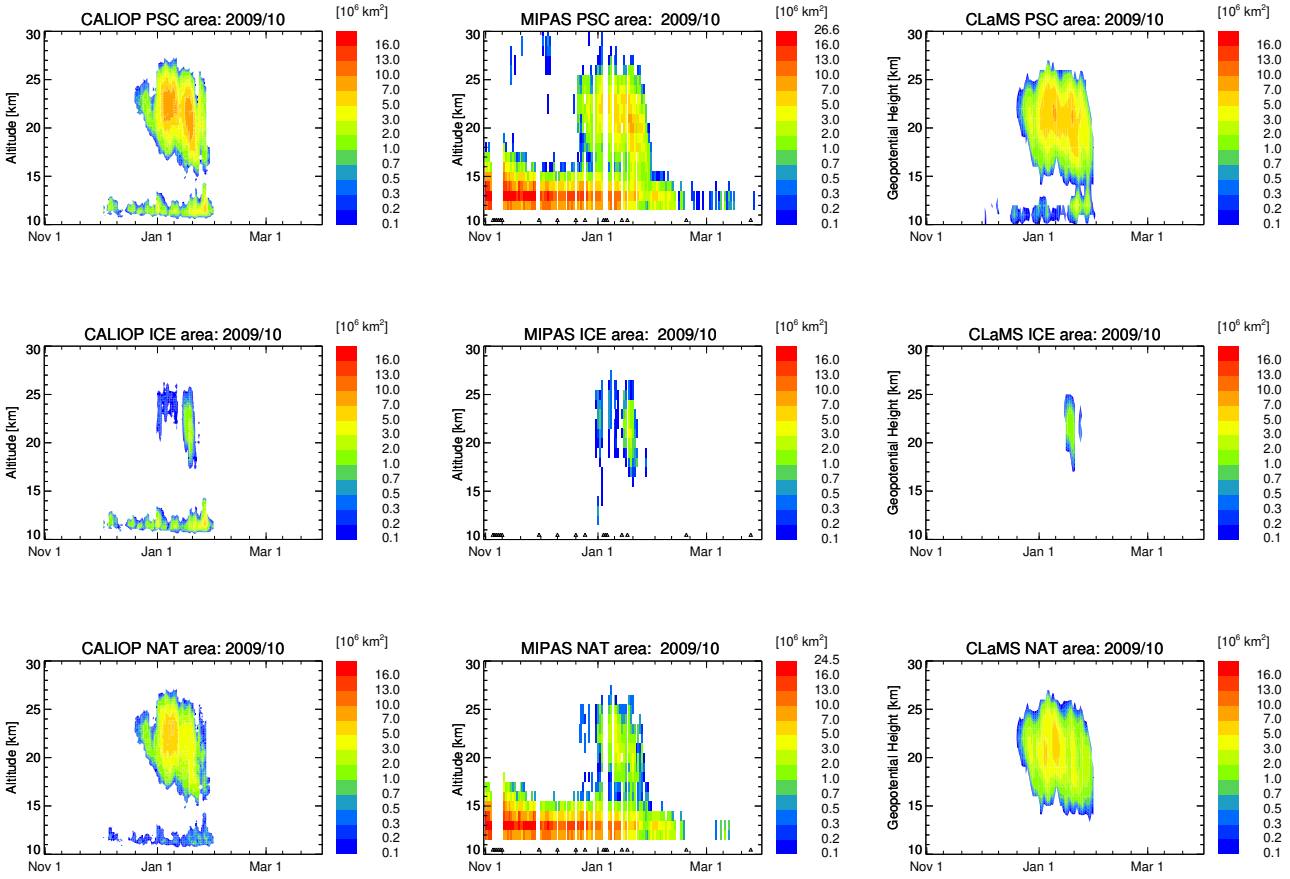

Figure 2. Comparison of PSC areal coverage between CALIOP (v2) left column, MIPAS (v1.2.8) middle column, and CLaMS right column from 01 December 2009 until 31 March 2010. Total PSC areal coverage (A_{PSC}) in $10^6\mathrm{km}^2$ (top row) as well as further classified ice (middle row) and NAT PSCs (bottom row) are presented as a function of time and altitude throughout the 2009/10 NH winter. MIPAS observations and CLaMS simulations are restricted to latitudes $< 82°$ N. PSC thresholds for CLaMS simulations are as follows: STS: $3.3\,\mu\mathrm{m}^2\mathrm{cm}^{-3}$, NAT: $0.25\,\mu\mathrm{m}^2\mathrm{cm}^{-3}$, ice: $0.5\,\mu\mathrm{m}^2\mathrm{cm}^{-3}$. Black triangles in the time series of the measurements are indicating data gaps. Please note that the color code is always identical except the maximum value.

Atmos. Chem. Phys. Discuss., https://doi.org/10.5194/acp-2018-337
Manuscript under review for journal Atmos. Chem. Phys.
Discussion started: 15 May 2018
© Author(s) 2018. CC BY 4.0 License.

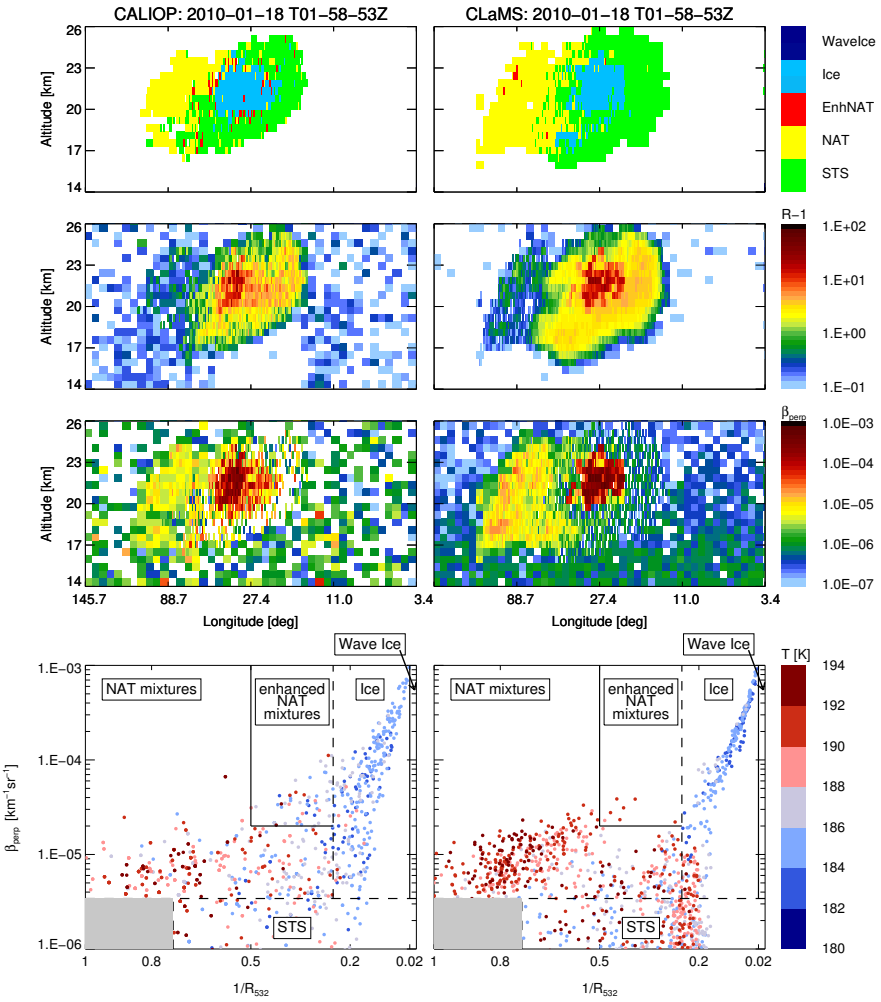

Figure 3. 18 January 2010: CALIPSO orbit track 2010-01-18T01-58-53Z. CALIOP measurements are shown in the left column, corresponding model results in the right column. First row: CALIOP PSC classification v2; second row: aerosol backscatter ratio ($R-1$); third row: perpendicular backscatter signal (β_{perp}); lowermost row: inverse backscatter ratio ($1/R$) vs. perpendicular backscatter signal (β_{perp}) with data color-coded by temperatures taken from GEOS-5 and ERA-Interim for CALIOP and CLaMS, respectively, and overlaid CALIOP v2 PSC composition classification scheme.

Atmos. Chem. Phys. Discuss., https://doi.org/10.5194/acp-2018-337
Manuscript under review for journal Atmos. Chem. Phys.
Discussion started: 15 May 2018
© Author(s) 2018. CC BY 4.0 License.

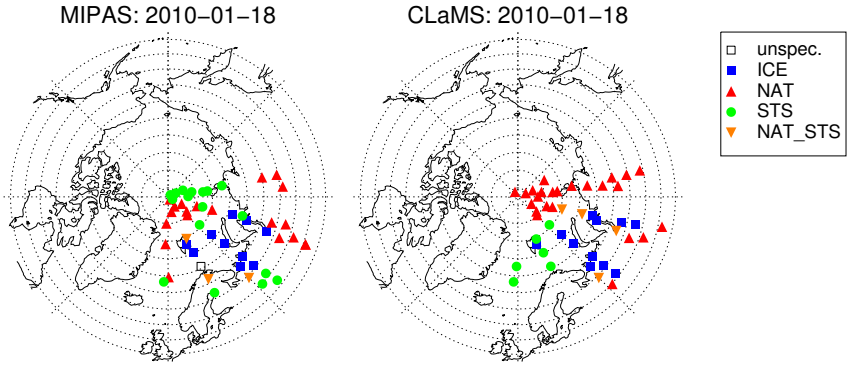

Figure 4. Horizontal distribution of MIPAS (left) and CLaMS (right) PSC composition classes for 18 January 2010 at an altitude level of 500 K ($\pm$ 20 K) potential temperature.

Atmos. Chem. Phys. Discuss., https://doi.org/10.5194/acp-2018-337
Manuscript under review for journal Atmos. Chem. Phys.
Discussion started: 15 May 2018
© Author(s) 2018. CC BY 4.0 License.

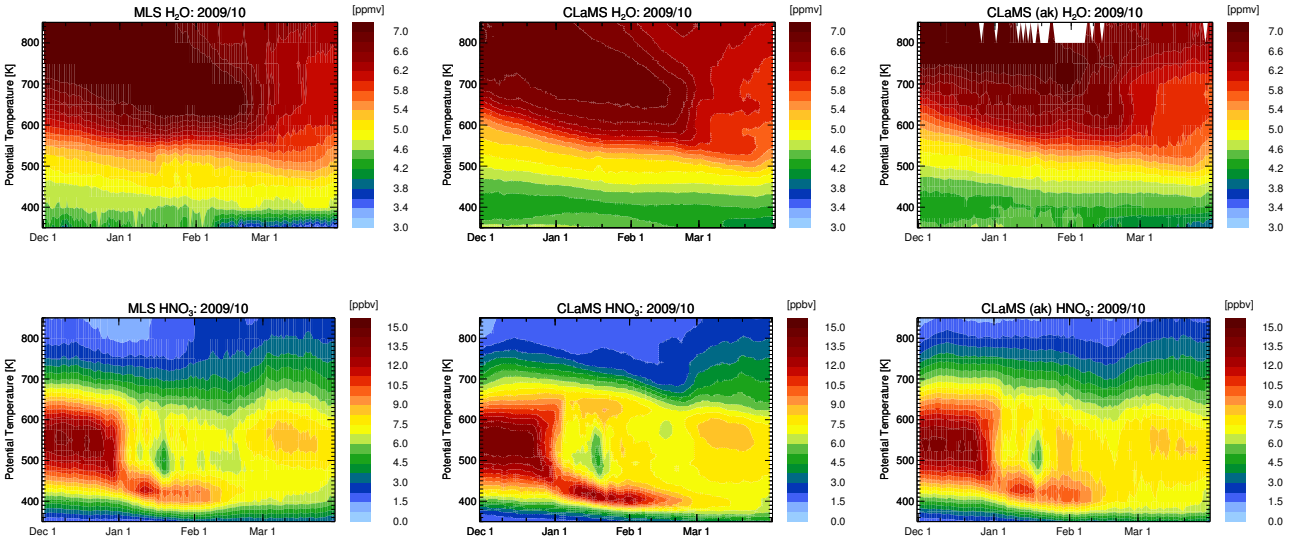

Figure 5. Temporal evolution of water vapor (H_2O, top row) and nitric acid (HNO_3, bottom row) are shown as an average inside the core of the polar vortex (equivalent latitudes $> 70°$ N) from 01 December 2009 until 31 March 2010. MLS measurements are presented in the left column, CLaMS model results in the middle column and CLaMS model results accounting for the MLS averaging kernel in the right column.

Atmos. Chem. Phys. Discuss., https://doi.org/10.5194/acp-2018-337
Manuscript under review for journal Atmos. Chem. Phys.
Discussion started: 15 May 2018
© Author(s) 2018. CC BY 4.0 License.

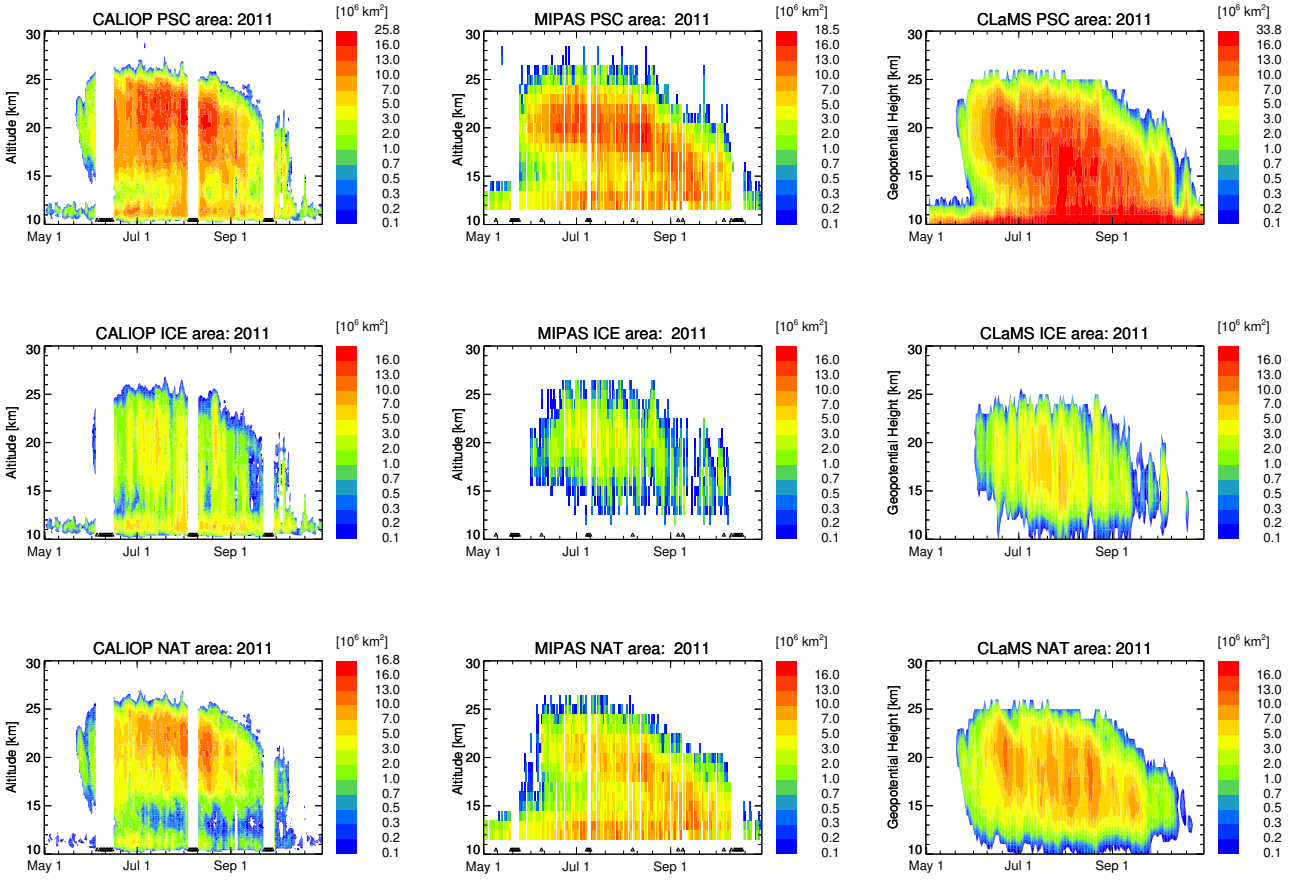

Figure 6. Same as Fig. 2 but for the 2011 SH winter from 01 May 2011 until 31 October 2011. Here, MIPAS observations and CLaMS simulations are restricted to latitudes $< 82^\circ$ S.

Atmos. Chem. Phys. Discuss., https://doi.org/10.5194/acp-2018-337
Manuscript under review for journal Atmos. Chem. Phys.
Discussion started: 15 May 2018
© Author(s) 2018. CC BY 4.0 License.

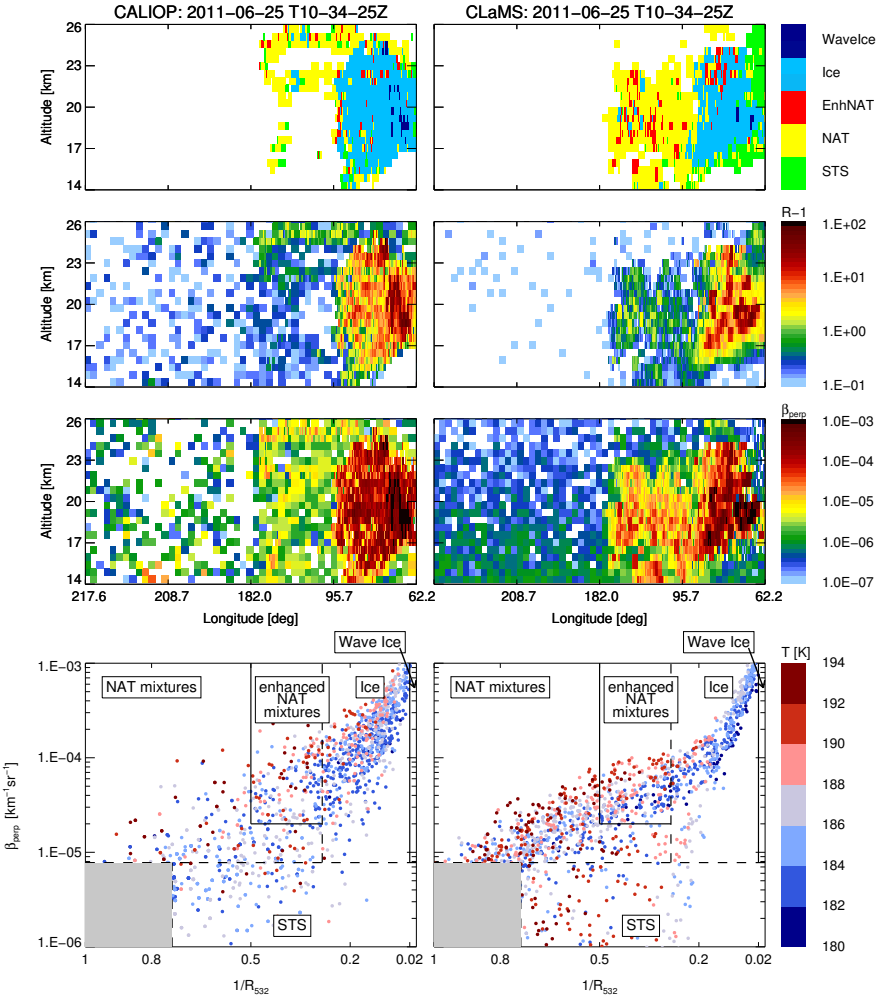

Figure 7. Same as Fig. 3 but for 25 June 2011: CALIPSO orbit track 2011-06-25T10-34-2Z.

Atmos. Chem. Phys. Discuss., https://doi.org/10.5194/acp-2018-337
Manuscript under review for journal Atmos. Chem. Phys.
Discussion started: 15 May 2018
© Author(s) 2018. CC BY 4.0 License.

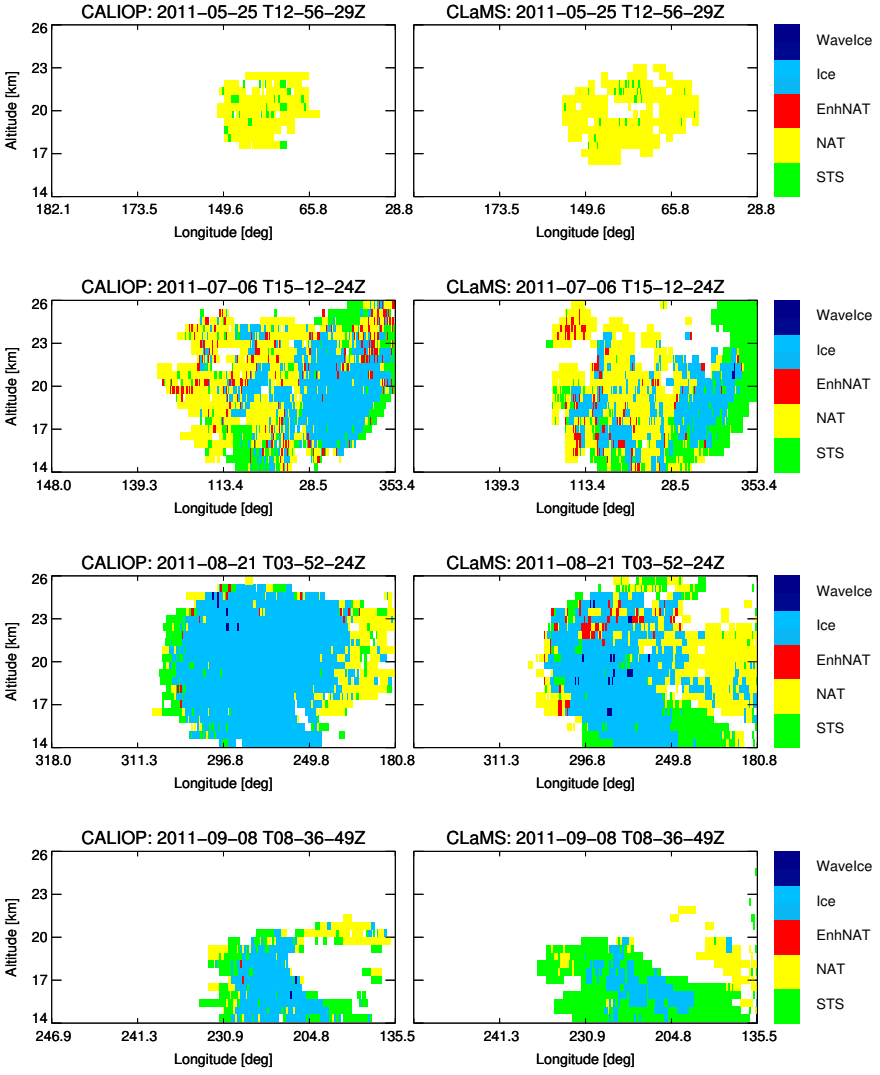

Figure 8. Same as first row in Figs. 3 and 7 but for four certain days in SH winter 2011: 25 May (2011-05-25 T12-56-29Z), 06 July (2011-07-06 T15-12-24Z), 21 August (2011-08-21 T03-52-24Z), 08 September (2011-09-08 T08-36-49Z).

Atmos. Chem. Phys. Discuss., https://doi.org/10.5194/acp-2018-337
Manuscript under review for journal Atmos. Chem. Phys.
Discussion started: 15 May 2018
© Author(s) 2018. CC BY 4.0 License.

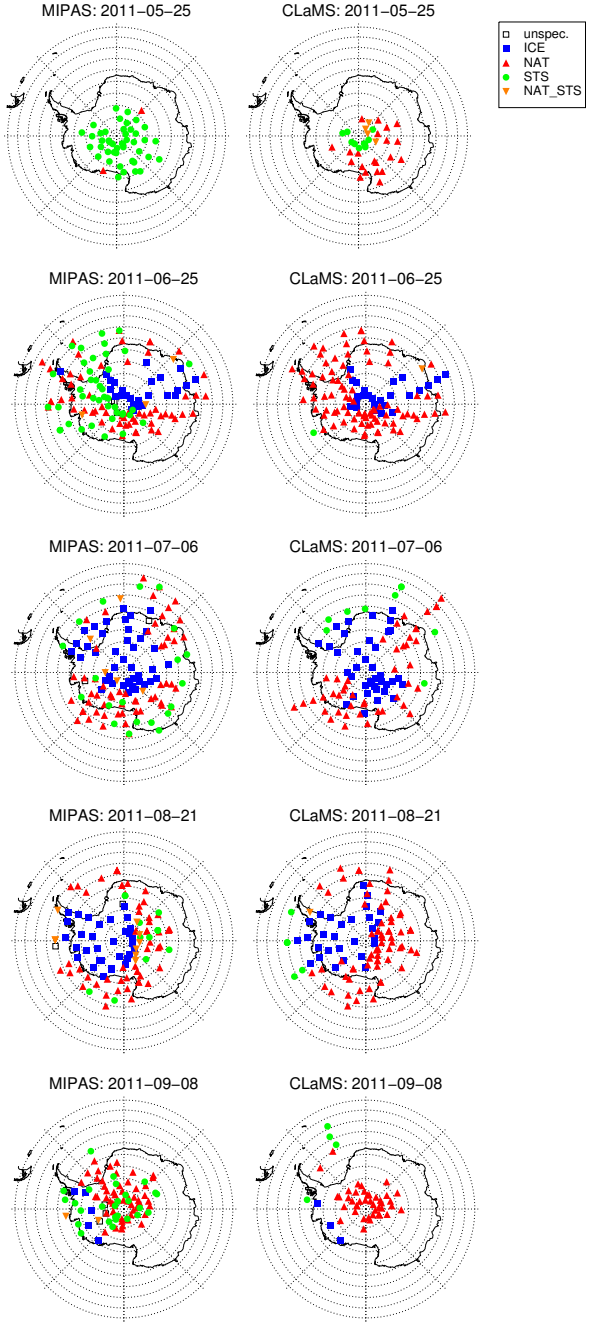

Figure 9. Same as Fig. 4 but for certain days in SH winter 2011: 25 May, 25 June, 06 July, 21 August, 08 September.

Atmos. Chem. Phys. Discuss., https://doi.org/10.5194/acp-2018-337
Manuscript under review for journal Atmos. Chem. Phys.
Discussion started: 15 May 2018
© Author(s) 2018. CC BY 4.0 License.

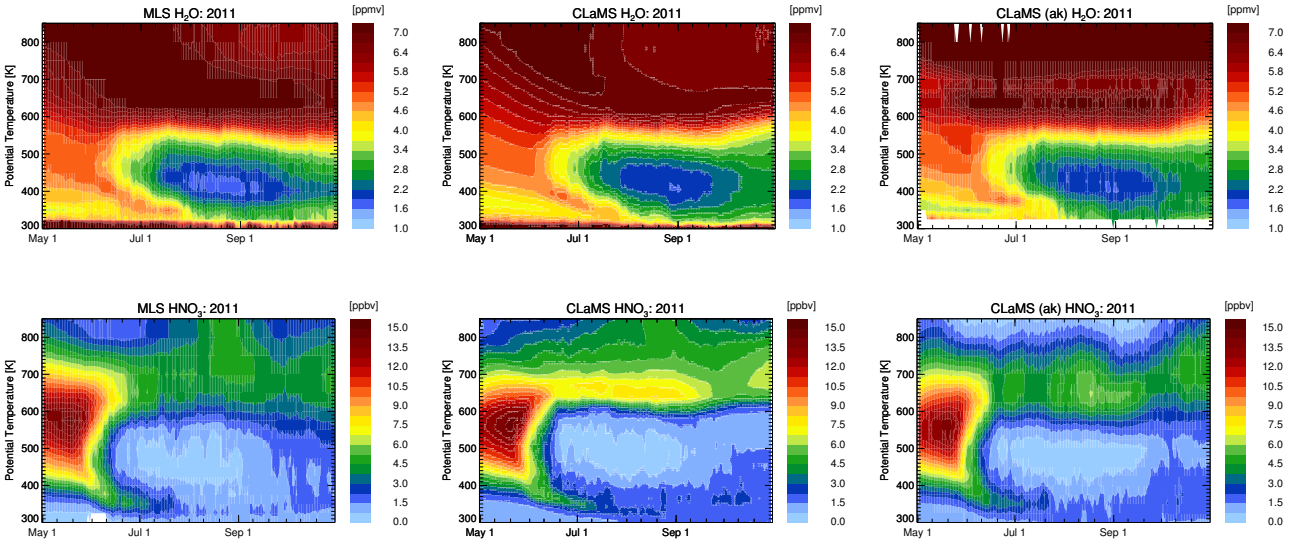

Figure 10. Same as Fig. 5 but for the 2011 SH winter from 01 May 2011 until 31 October 2011 and for equivalent latitudes $> 70°$ S.